

ELM Energy Losses in Peeling Limited Pedestals in JET

Victor Maloisel

June 2024

Abstract

Nuclear fusion is a research topic that attracts a lot of interest. If properly harnessed, it promises to be an energy source that circumvents problems that current energy sources have. As such, fusion warrants research aimed at understanding and dealing with its varied issues.

Fusion is regularly recreated on earth by heating a hydrogen plasma to around a hundred million degrees Celsius. Confining this plasma requires special machines due to the extreme heat. There are multiple types of machines recreating plasma for research purposes, the most common is called tokamak. Tokamaks confine the plasma in a toroidal shape using powerful magnetic fields that prevent particles from escaping. Relevant for this work is the tokamak JET, where the treated experiment has been conducted, and ITER, which is currently under construction and meant to be the next step in fusion research.

An important phenomenon are so called Edge Localized Modes (ELMs). ELMs are short bursts of energy expulsions from the plasma that results in a loss of energy and can cause damage to components facing the plasma. While not necessarily present in all operational modes ELMs are present in JET and will be present in ITER. Therefore it is very important to understand ELMs and how they are affected by certain parameters. Especially important is the dependency of ELM size on collisionality, a measurement on how much particles in the plasma interact with each other. Due to how ITER is supposed to operate it will have a very low collisionality, something that previous studies have linked with large ELM energy losses. This work investigates how parameters, plasma density, gas fueling rate, effective mass, strength of the magnetic field and collisionality affect ELMs.

This work calculates the energy losses for ELMs and investigates whether they are related to certain parameters. To calculate the energy loss two methods are deployed. One method relies on measurements of the diamagnetic flux. The other utilizes measurements of temperature and density with thomson scattering, electron cyclotron emission and reflectometry. Both techniques compare the energy in the plasma before and after an ELM to deduce the energy loss. For both methods, ELMs in a time interval are grouped and their data is used to calculate a typical energy loss.

The results show that the energy losses from both methods are comparable with previous measurements at similar collisionality. The methods produce comparable results although the results for singular cases are not always in agreement. Ion cyclotron resonance heating is identified as worsening the agreement. A combination of the results being too noisy and there not being enough data means that no clear trends were observed in the investigated parameters.

Keywords: Fusion, Pedestal, ELM, JET, ITER

Sammanfattning

Fusion är ett intressant forskningsområde. Om det nyttjas på rätt sätt, kan fusion bli en energikälla kringgår problem som nuvarande energikällor har. Därför finns det mycket forskning om fusion med målet att förstå och hantera de problem som idag stoppar fusion från att användas som energikälla.

Fusion återskapas på jorden genom att värma väteplasma till cirka hundra miljoner grader Celsius. Att hålla plasmat kräver speciella maskiner på grund av den extrema värmen som lätt smälter alla material. Det finns flera olika maskiner som kan upprätthålla plasma för forskningsändamål, även om de ännu inte kan utvinna energi. Den vanligaste kallas tokamak. Tokamaker håller plasmat i en toroidal form med hjälp av kraftiga magnetfält. För detta arbete är tokamakerna JET och ITER relevanta. Datan som behandlas i detta arbete kommer från JET. ITER är en forskningsreaktor som är under konstruktion och är ämnad att vara nästa steg inom fusionforskning.

Ett viktigt fenomen är Edge Localized Modes (ELMs). ELMs är korta energipulser från plasmat som kan orsaka skador på komponenter vända inåt mot plasmat. ELMs är inte nödvändigtvis närvarande men de är närvarande i JET och kommer att vara närvarande i ITER. Därför är det viktigt att förstå dem. Särskilt viktigt är hur ELM-storleken ändras beroende på kollisionslitenhet, ett mått på hur mycket partiklar i plasmat interagerar med varandra. På grund av hur ITER ska köras kommer kollisionslitenheten vara mycket låg, något som tidigare studier har kopplat till stora ELMs. Beroende på vad som utlöser en ELM säger man att de är peeling eller ballooning begränsade. De flesta experimenten idag är ballooning-limited, vilket betyder att ELMs utlöses på grund av en för hög tryckgradient. På grund av den låga kollisionslitenheten tros ITER bli peeling-limited, vilket betyder att ELMs utlöses av för höga strömmar i plasmat. I ett försök att härma ITERs operationstillstånd har experimentet som undersöks i detta arbete låg kollisionslitenhet. De parametrar vars inflytande på ELMs undersöks är plasmats densitet, bränsletillförsel, effektiv massa, styrkan av magnetfältet och kollisionslitenhet.

För att beräkna energiförlusten används två metoder, en använder en mätning av magnetflödet i plasmat. Den andra metoden använder mätningar av temperaturen och densiteten vid punkter i plasmat. Båda teknikerna jämför energin i plasmat före och efter en ELM för att fastställa energiförlusten. För båda metoderna används alla ELMs under en period för att beräkna en karaktäristisk energiförlust.

Energiförlusterna är jämförbara med tidigare mätningar vid liknande kollisionslitenhet. De använda metoderna ger överlag liknande resultat för de olika undersökta intervallen. Ion Cyclotron Resonance Heating (ICRH) identifieras förvärra överensstämmelsen avsevärt. En kombination av att resultaten har hög osäkerhet och att det finns få datapunkter innebär att tydliga trender inte observerades i de undersökta parametrarna.

Nyckelord: Fusion, Pedestal, ELM, JET, ITER

Acknowledgements

First of all, I want to thank my supervisor, Lorenzo Frassinetti. Despite having a busy schedule, you have always been supportive and taken time to give me helpful feedback quickly. Not only was the project very interesting, but you were always clear on what I should do. Working towards a clear goal with well-defined boundaries has made writing my master's thesis with you as my supervisor a pleasure.

I want to thank Hampus Nyström. Your explanations of everything from plasma physics to scientific writing conventions have allowed me to learn a lot in a very efficient and stress-free manner. I am also grateful for your patience in reading and commenting on multiple early and poor versions of this work. Your experienced perspective and insightful explanations have saved me a lot of stress and time, and doubtlessly improved my work.

I also want to thank my family and friends. Some of you have helped me relax and gain much-needed distance from my work when I have been stressed or dismayed. Others have made even long and demanding days pleasant through their company. All of your support has helped me immensely.

Contents

| | | |
|----------|--|-----------|
| 1 | Introduction | 6 |
| 1.1 | Background | 6 |
| 1.2 | Fusion | 7 |
| 1.3 | Tokamak | 9 |
| 1.4 | Magnetohydrodynamics | 10 |
| 1.5 | H-mode and the pedestal | 12 |
| 1.6 | Edge localized modes | 13 |
| 1.7 | ELMs in ITER | 16 |
| 1.8 | Thesis objective | 18 |
| 2 | Theory | 18 |
| 2.1 | Parameters | 18 |
| 2.2 | Diagnostics | 20 |
| 2.2.1 | Thomson scattering | 20 |
| 2.2.2 | Reflectometry | 20 |
| 2.2.3 | Electron cyclotron emission | 21 |
| 2.2.4 | Diamagnetic energy | 21 |
| 2.2.5 | Interferometry | 21 |
| 2.2.6 | Beryllium recombination line emission | 21 |
| 3 | Method | 22 |
| 3.1 | ELM selection | 22 |
| 3.2 | Profile fitting | 22 |
| 3.3 | Energy loss from profiles | 24 |
| 3.4 | Energy loss from W_{dia} | 27 |
| 3.5 | Pedestal stored energy and normalization | 28 |
| 3.6 | Data Set | 31 |
| 4 | Results | 35 |
| 4.1 | Comparison of moving averages and window averages | 35 |
| 4.2 | Comparison of diamagnetic measurements and profile fitting | 35 |
| 4.3 | Comparison between convective and conductive losses | 38 |
| 4.4 | Dependencies on collisionality | 39 |
| 4.5 | Dependencies on magnetic field strength | 41 |
| 4.6 | Dependencies on density | 42 |
| 4.7 | Dependencies on gas fueling rate | 43 |
| 4.8 | Dependencies on effective area | 45 |
| 5 | Discussion | 48 |
| 6 | Appendix | 51 |
| 6.1 | Discussion on problematic time interval | 51 |

1 Introduction

This section aims to present the context of this work. Firstly the need for fusion is discussed. Secondly the concept of fusion is introduced. This is followed by explanations of some important concepts for fusion in general and specifically for this work. Lastly the scope of this work is presented along with its importance for fusion research.

1.1 Background

There is a worrying trend that the global energy consumption is constantly increasing. Despite a rapid increase in the production of renewable energy, an increase in fossil fuel has been necessary to keep up with demands [1]. This is shown in **Fig. 1** which showcases the global energy consumption between 1993-2018. Fossil fuels already stands for a large portion of the worlds energy consumption and as such will be difficult to phase out. Nonetheless reducing our dependency on fossil fuel is important as it is a finite resource and its usage contributes to global warming.

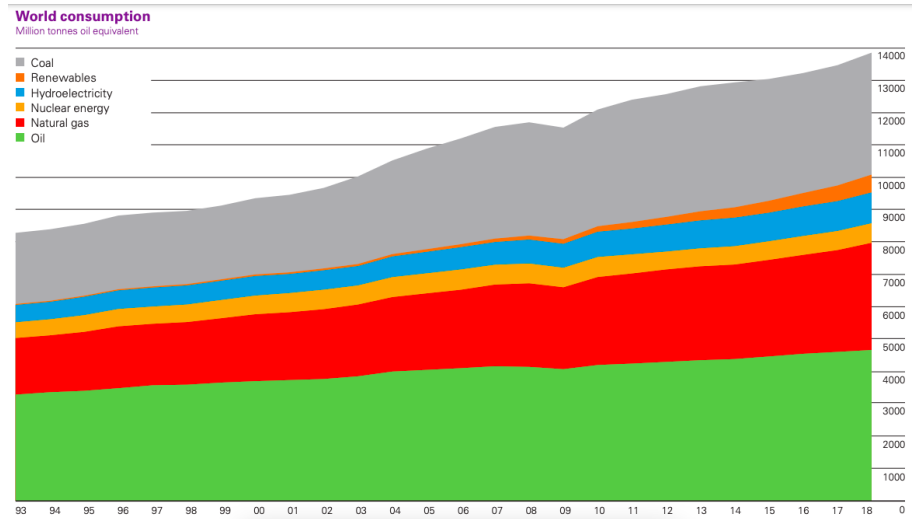


Figure 1: Global energy consumption in million tonnes oil equivalent per year, split between energy sources. Figure taken from [1].

There is an abundant amount of evidence for global warming and the scientific consensus is that it is caused by mankind. There has been an increase of 1.10°C in the global mean temperature between 2011-2020 as compared to 1850-1900. Despite this increase seeming modest, global warming has already been linked to an increase in risk for natural disasters such as, extreme heat waves, extreme cold, tropical cyclones, floods, droughts and wildfires [2]. Not only do these natural disasters result in costly damages but also forced migra-

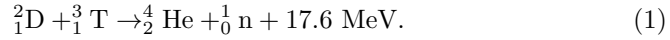
tion and even deaths. The burning of fossil fuel has been identified as a major contributing factor and as such has led to countries committing to phase out fossil fuels [3]. While there are alternative energy sources to fossil fuel, such as nuclear fission and renewable energy they are currently not enough to keep up with global demand on energy.

A promising future source of energy is nuclear fusion. Theoretically, fusion has many benefits compared to other energy sources. For one, the only fuel needed for fusion is deuterium and tritium. Deuterium is found in seawater and tritium can be produced from lithium which can also be extracted from seawater. Seawater is very abundant, making fusion a highly sustainable energy source [4]. Secondly there are no green house gas emission associated with fusion and as such it will not contribute to global warming. Thirdly, compared to fission, fusion has the advantage that it produces no long-lived radioactive waste which can be difficult to deal with. There is also no danger of a nuclear accident as there would be in a fission power station. This is because there is only a very small amount of fuel in the fusion reactor at any given time. The reactors rely on a continuous fuel flow to remain active and could therefore always be shut down by cutting off access to the fuel [5].

1.2 Fusion

Fusion is any reaction where two or more particles combine to produce one or multiple new particles, one of which is heavier than the previous particles. Already in the 1920s, fusion was theorized to be the energy source for stars. The theory was based on observations that some of lightest isotopes have lower mass per nucleon than heavier ones. By combining this discovery with the Einstens' then newly formulated relationship between mass and energy the first idea of fusion energy was created [6]. Since then a lot of progress has been made in nuclear fusion and today there are multiple devices capable of sustaining creating fusion.

The fusion reaction that is most important in fusion devices and hence the most important for this work is the fusion of deuterium and tritium creating helium and a neutron according to,



An important concept for this reaction is its cross-section. The cross-section, commonly denoted σ , is a measurement of how likely a reaction is to happen when particles collide. Fusion reactions such as the one described in **Eq. 1** are mediated by the strong force which is dominant at small distances. In order for the particles to reach these small distances, they must overcome the coulomb barrier caused by them both having a positive charge. If the particles have higher energy they are more likely to overcome the coulomb barrier. Therefore, the cross-section for fusion reactions increases with increasing temperature in the relevant temperature range.

Reactivity, which is based on the concept of cross-section, is another relevant quantity for fusion reactions. Denoted $\langle \sigma v \rangle$, it takes in to account both the

cross-section of a reaction and the average velocity of particles. The average velocity is included because faster moving particles have more chances to interact with other particles. As such, reactivity more accurately measures how prevalent reactions are compared to the cross-section. The reactivity for three possible fusion reactions is shown in **Fig. 2**. The temperature range that is relevant for current and future fusion reactors is somewhere > 10 keV. In this region, an increase in temperature results in an increased reactivity as both the cross-section and the average velocity of particles increases. This is reflected in **Fig. 2** where the reactivity of all three processes increase with temperature. The reason the reaction described in **Eq. 1** is favorable is because it has a higher reactivity than other reactions at reachable temperatures.

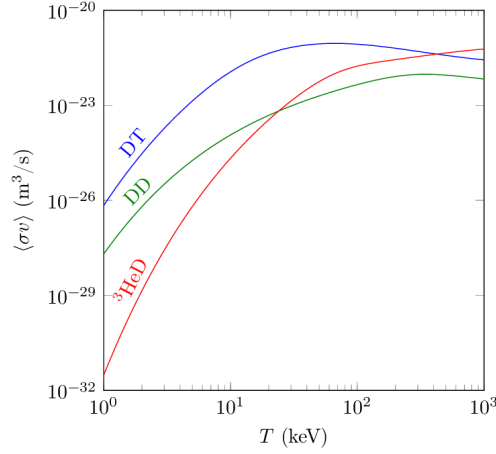


Figure 2: Reactivity for fusion reactions between deuterium and tritium, deuterium and deuterium and deuterium and helium-3. Figure taken from [7].

Another important factor for increasing the number of reactions is density. A greater concentration of particles leads to more frequent collisions and thus more reactions. Having a high density and a high temperature leads to a high pressure as the quantities are related according to,

$$p = k_b T n. \quad (2)$$

Here p is the pressure, k_b is the Boltzmann constant, T the temperature and n the number density. As can be seen in **Fig. 2**, the temperature with the highest reactivity is somewhere around 10^4 eV which corresponds to 10^8 K. No materials are able to withstand such heat and so other methods of confinement are necessary. Luckily, at these high temperatures the fuel is completely ionized, meaning that the nuclei and the electrons are detached from each other. This means that the particles in the plasma are all electrically charged. Multiple concepts of fusion devices utilizes the electrical charge of particles to confine the plasma with magnetic fields. The magnetic field exerts a force on the particles

equivalent to,

$$F = q\vec{v} \times \vec{B}, \quad (3)$$

This means that any velocity perpendicular to the magnetic field lines results in a force deflecting the particle while any velocity along the magnetic field lines is unaffected. The result is that all charged particles move in a helical trajectory along the magnetic field as long as the magnetic field is constant. By manipulating the shape of the magnetic field it can thus be used to confine a plasma.

Today there are multiple different types of devices able to create, sustain and confine plasma at temperatures and densities where fusion reactions occurs. The data treated in this work comes from the Joint European Torus (JET). Since its first experimental campaign in 1983, JET has been on the forefront of fusion research and played a crucial role in developing our current understanding. In December 2023, after 40 years of running, JET had its final experiment and has since been closed [8].

Also relevant to this work is the International Thermonuclear Energy Reactor (ITER) which is currently under construction. ITER is a collaboration of 35 countries across the world and is meant to be the next step in fusion research. With a plasma volume of 840 m³, one of ITERs main advantages will be its size which is almost ten times larger than that of most other reactors. Additionally, ITER is supposed to sustain plasmas at 150 million °C and generate 500 MW [9], corresponding to 10 times the heating required by the plasma [10].

1.3 Tokamak

The tokamak is the most common type of fusion reactor and both JET and ITER are based on its concept. The name, tokamak, comes from the Russian expression for toroidal chamber with magnetic coils. As the name suggests, the tokamak confines the plasma inside of a toroidal chamber with powerful magnetic fields[11]. The toroidal shape is demonstrated in **Fig. 3**. Important for understanding this work is the toroidal direction, shown in blue, and the poloidal direction, shown in red.

To avoid heat leakage and unwanted interactions between the plasma and its surroundings the chamber is pumped to near perfect vacuum before the start of any experiment. Once a vacuum state is reached, the magnetic fields that hold the plasma in place are activated and the gas fuel is introduced [11].

Tokamaks utilizes a strong magnetic field in the toroidal direction generated by multiple magnetic coils. The toroidal magnetic field is the main component of the total magnetic field and its magnetic field lines close upon themselves. If the toroidal field would be perfectly constant, all electrically charged particles would follow its magnetic field. This would effectively trap the particles in a helical path around the plasma in the toroidal direction so that they do not leave the plasma.

The magnetic field is, however, not constant with only a toroidal field. Instead, the toroidal shape of the chamber creates a slight gradient in the magnetic

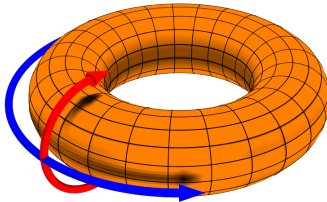


Figure 3: Figure showcasing the shape of a toroid. The toroidal direction is represented by the blue arrow and the poloidal direction is represented by the red arrow. Figure taken from [12].

field. Because of the gradient, particles tend to drift differently based on their charge creating a separation between electrons and ions. The separation causes local charge concentrations and electrical fields appear that worsens the stability of the plasma.

To counteract the drift, a poloidal magnetic field is superimposed on the toroidal magnetic field. To achieve the poloidal field, coils placed in the middle of the toroid induce a current in the plasma in the toroidal direction. The current in turn generates the main part of the poloidal magnetic field. Finally the outer poloidal field coils are added in order to shape and position the plasma when necessary [13].

The described magnetic field along with the coils creating it are shown in **Fig. 4**. An example of how the total magnetic field might appear is also shown. Its main component is in the toroidal direction but it also has a non-negligible component in the poloidal direction.

1.4 Magnetohydrodynamics

The plasma is a much too complicated system to be described as individual particles effectively. As such, some simplifications are necessary to create an effective model of the plasma. One such simplification is to describe the plasma as one electrically conducting fluid, ignoring that it consists of ions and electrons. This is the basis for magnetohydrodynamics (mhd) in which the plasma is described using macroscopic quantities such as temperature, pressure and density at spatial coordinates. The equations on which magnetohydrodynamics is based is a mixture of Navier-Stokes equations to describe the plasma as a fluid and Maxwell equations to describe the electromagnetical characteristics of the plasma [14]. The most relevant equation of magnetohydrodynamics for this work is the force balance equation,

$$\vec{J} \times \vec{B} = \nabla p. \quad (4)$$

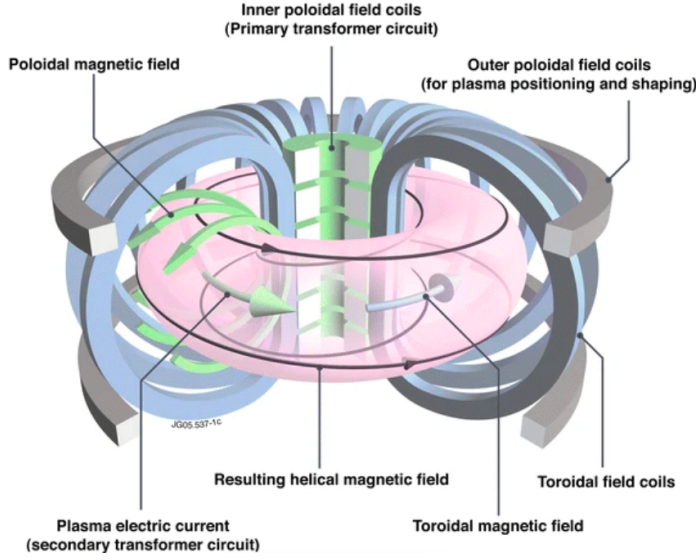


Figure 4: Schematic view of the configuration of magnetic coils along with the resulting magnetic fields. Figure taken from [13].

The above equation implies that the pressure only changes along the direction perpendicular to the current and the magnetic field since, $\vec{J} \cdot \nabla p = 0$ and $\vec{B} \cdot \nabla p = 0$ [15]. The pressure is thus constant on the surface spanned by magnetic field lines and the current. These surfaces are called flux surfaces. Additionally, it can be proven that the temperature and density is constant on flux surfaces. These surfaces are not necessarily at a constant distance from the magnetic center of the plasma as can be seen in **Fig. 5** which shows a schematic cross-section of plasma in a tokamak with flux surfaces marked. This makes polar coordinates a poor choice for describing temperatures and pressures in a cross section.

Instead what can be used is the poloidal magnetic flux. This quantity is constant along a flux surface and strictly growing when moving away from the center of the plasma. Thus the poloidal flux is useful as a coordinate. In this work the coordinate has been normalized such that it has value 0 in the center of the plasma and 1 at the separatrix of the plasma. The separatrix is a flux surface that crosses itself and is marked as main separatrix in **Fig. 5**. Inside of the separatrix all flux surfaces are closed, while outside of it all flux surfaces are open [16]. Each flux surface is a two dimensional surface stretching around the plasma. By finding the areas these surfaces cover one can calculate $\frac{dV}{d\psi}$ to relate flux coordinates to a volume. Outside of the separatrix this is not possible as the surfaces are not closed and thus infinite. The plasma outside of the separatrix is called the Scrape Off Layer (SOL).

The main benefit of using flux coordinates is that a measurement of temperature or density can be extrapolated to an entire flux surface. As such, one

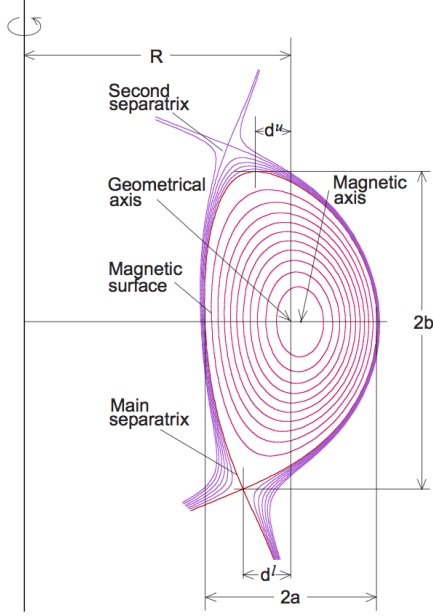


Figure 5: Schematic view of the cross-section of a plasma with magnetic surfaces highlighted. Figure taken from [16]

does not have to measure these quantities on all points of interest. Additionally, temperature and density can be measured at different physical locations and still be compared to each other.

1.5 H-mode and the pedestal

Plasmas can operate in different modes, most relevant for this work is the high confinement mode (H-mode). Plasmas will transition from low confinement mode (L-mode) to H-mode once a threshold power is achieved. H-mode is desirable as it allows for higher temperature and density in the plasma compared to L-mode. In fact, while the plasma remains in L-mode, increased heating leads to decreased energy confinement. This means that high temperatures are unattainable in L-mode [17].

The main characteristic of H-mode plasma is that there is a narrow region at the edge where the gradient of the pressure is larger than in the rest of the plasma [18]. Similar regions can exist both in temperature and density independently.

For the region enclosed by the edge, both H-mode and L-mode have very similar gradients. The result is that the edge region increases these quantities throughout the profile. The edge region is called a pedestal because it causes the profile to be raised by a near constant amount compared to the compared

L-mode profile, as if it rests on a pedestal. A schematic comparison between H-mode and L-mode can be seen in **Fig. 6** where the elevating effect of the pedestal has been highlighted.

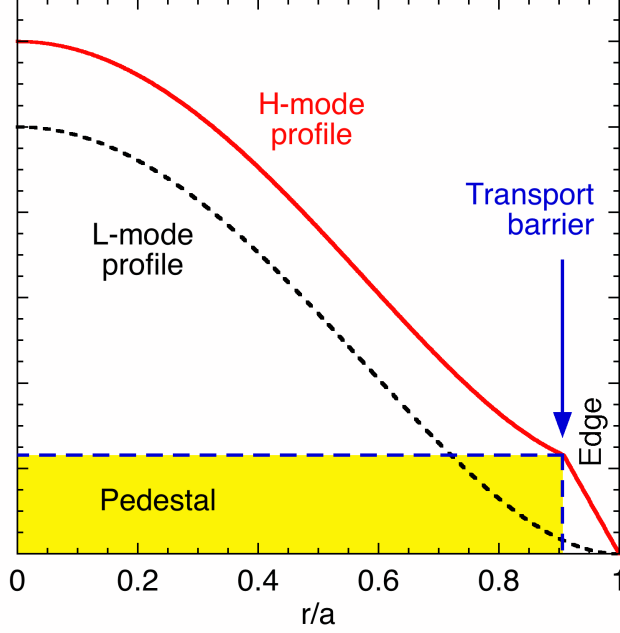


Figure 6: Schematic view of how the pressure, density and temperature typically looks as a function of the radius in a plasma. Both typical H-mode and L-mode profiles are shown and the difference caused by the pedestal is highlighted. Figure is taken from [19]

The transition from H-mode to L-mode is caused by the formation of a transport barrier at the edge of the plasma, just inside of the separatrix. The transport barrier greatly reduces the turbulent transport of particles which is dominant in the pedestal region. The result of the transport barrier is that the pressure gradient in this region can grow higher [20]. The latest research seems to indicate that a transport barrier is formed due to a radial electric field. The electric field, in turn causes a drift velocity, $\vec{E} \times \vec{B}$, which shears instabilities, stopping their growth and allowing for higher pressure gradients [21].

1.6 Edge localized modes

While operating in the H-mode, the edge region of plasmas has been observed to periodically collapse. The collapse results in a loss of energy as both heat and particles are lost from the plasma. These events are called Edge Localized Modes (ELMs).

A typical loss of temperature and density over an ELM can be seen in **Fig. 7**. Note that the losses are concentrated in the pedestal region. By comparing the profiles before and after ELMs one can see that the sharp gradient that is characteristic for the H-mode collapses. The resulting profiles have lower density and temperature in the pedestal region. Meanwhile, the density increases outside of the separatrix, indicating that particles are pushed out of the plasma to the scrape of layer[22].

The plasma treated in this work operates in ELMy H-mode, meaning that ELMs are regularly triggered. The ELMs typically happen on a timescale of less than a millisecond with a periodicity of somewhere between 5 – 100 ms, making most ELMs distinguishable as separate events [23].

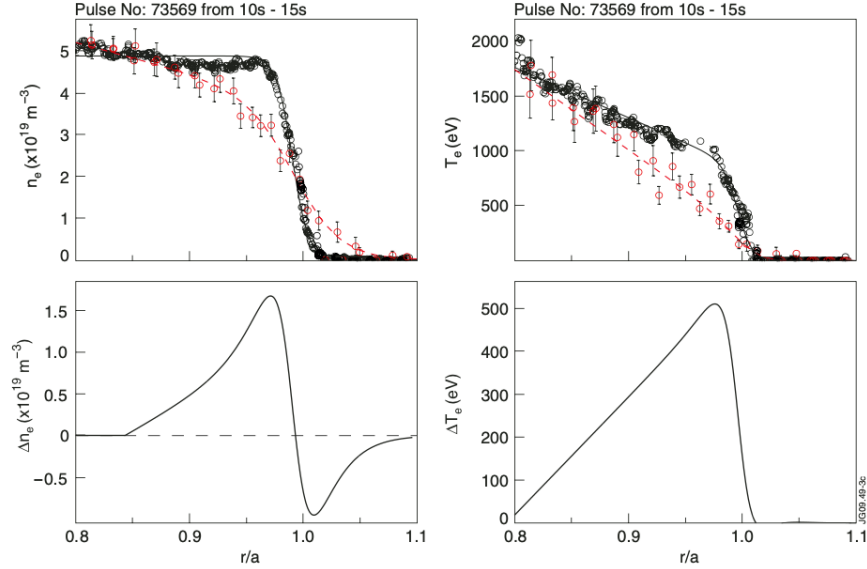


Figure 7: The top left figure shows the density profile right before an ELM (black) and right after an ELM (red). The top right figure shows the temperature profile right before an ELM (black) and right after the an (red). The bottom figures show the difference between the fitted curves for density and temperature in the left and right figures respectively. Figure taken from [22]

Through simulations using magnetohydrodynamics, predictions can be made on how large the pressure gradient and pedestal current can grow before an instability is triggered. Once the pressure gradient or the pedestal current exceeds its limit, an ELM is triggered. When plotted in the current density versus pressure gradient space, the limits form boundaries that enclose a region where the plasma is stable. Based on whether the ELM is triggered by the pressure gradient or current the ELM is called ballooning or peeling respectively. A schematic depiction of the boundaries and the stability region they form is shown in **Fig. 8**. This model of plasma stability is called peeling-ballooning and describes type

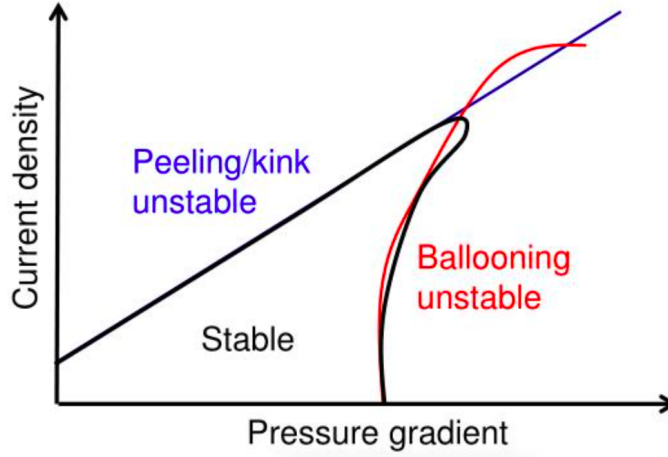


Figure 8: A schematic figure of the stability region in shown in current density versus pressure gradient space. Taken from [25].

I ELMs well. While there are other types of ELMs they are not relevant for this work and as such are not described here. JET and most european fusion experiments operate at the ballooning limit. As such, comparatively little is known about ELMs at the peeling boundary [24].

Each ELM results in a collapse in the pressure profile, causing the plasma to move away from the pressure gradient limit. In the pedestal region, a significant part of the current is bootstrap current which is generated by the pressure gradient. As such the pressure loss also results in a decrease in the bootstrap current and therefore also the total current. After an ELM, pedestal is rebuilt back up. Eventually, the plasma once again reaches a stability limit, at which point an ELM is triggered and the cycle restarts. The plasma is called peeling- or ballooning-limited, depending on whether the instabilities arise from the current or pressure gradient respectively.

The main problem with ELMs is that they expel large amounts of energy. Through this, each ELM damages the fusion machines components that are facing the plasma. Conversely, the high pressure gradients in the edge means a higher pressure profile throughout the plasma, which means a higher reaction rate. As such, H-mode seems necessary for effective fusion, despite its drawbacks.

ELMs also have benefits for the plasma. Over time, plasma impurities from the wall facing the plasma, as well as helium created through fusion, will dilute the plasma. This dilution slows down the fusion reactions. These impurities will also increase the radiative losses from the plasma and worsens its ability to retain heat [14]. The ELMs reduce the amount of impurities by periodically expelling particles, including impurities, from the plasma. Therefore, H-mode with ELMs is the most common operational mode. Due to the build up of

impurities, no H-mode without ELMs has been successfully sustained a longer time [18]. It is by operating in ELMy H-mode that ITER has been predicted to be able to yield an energy return of 10 times the invested energy [17].

1.7 ELMs in ITER

While ELMs are not very problematic in current fusion machines, some predictions project them to be much worse in ITER. To understand why, one needs to examine the concept of collisionality. The collisionality of a plasma is a measurement of how much particles interact with each other. For a plasma with low collisionality, particles will mostly follow the magnetic field lines. In a plasma with high collisionality the particle interactions with each other are dominant, making its characteristics more like that of a gas.

For this work, normalized pedestal collisionality is used. The pedestal collisionality is calculated at the top of the pedestal and assumed to represent the collisionality of the whole pedestal. Normalized pedestal collisionality, ν^* is calculated as,

$$\nu^* = 6.921 \cdot 10^{-18} \ln \Lambda \frac{R q_{95} n_e^{ped}}{\varepsilon^{3/2} (T_e^{ped})^2}. \quad (5)$$

Here R is the major radius of the cross-section of the plasma, q_{95} is the safety factor at $\psi = 0.95$, n_e^{ped} and T_e^{ped} is the electron temperature and density at the pedestal respectively and $\varepsilon = \frac{R}{r}$ where r is the minor radius of the plasma. Lastly, $\ln \Lambda$ is calculated according to **Eq. 6**.

$$\ln \Lambda = 31.3 - \ln \frac{\sqrt{n_e^{ped}}}{T_e^{ped}} \quad (6)$$

The previously mentioned safety factor, denoted q , measures how much the magnetic field turns around the toroidal axis and is calculated according to,

$$q = \frac{\text{number of toroidal turns}}{\text{number of poloidal turns}}. \quad (7)$$

Where the number of poloidal and toroidal turns refers to the amount of turns made in respective direction before closing on itself again, that is, when it has the same poloidal and toroidal coordinate as in the beginning. However, magnetic fields do not necessarily close. As such, the safety factor is practically calculated as the inverse of the fraction of a poloidal turn a magnetic field line has done after one toroidal turn. The safety factor is important as it compares the strength of the toroidal magnetic field to the poloidal magnetic field.

Many predicted parameters in ITER are unattainable in current reactors. Because collisionality is normalized, the size difference and other differences in operational parameters can be accounted for [26]. Additionally, the normalization of collisionality allows for dependencies to be found using data from different machines. These dependencies can be extrapolated to the collisionality at which ITER will operate and as such a prediction on the size of ITERs

ELMs can be made. ITER is predicted to operate at low collisionality compared to currently operating fusion devices [10]. By plotting the energy losses against collisionality as is done in **Fig. 9**, a clear trend emerges in which low collisionality implies large ELM losses. In **Fig. 9** data from multiple machines have been utilized. To account for differences in plasma stored energy, the ELM losses have also been normalized. The ELM energy losses are normalized by dividing with the pedestal stored energy. The pedestal stored energy is the amount of energy the plasma gains by having a pedestal, see **Sec. 1.5**. How the pedestal stored energy is calculated is described in **Sec. 3.5**.

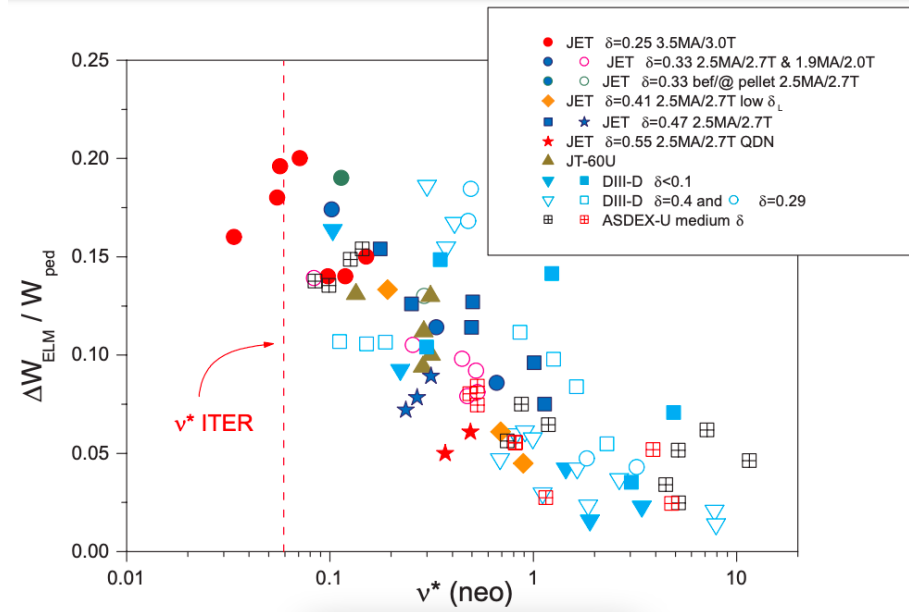


Figure 9: The normalized energy losses from ELMs is plotted against normalized collisionality. Different experiments and machines are shown in different shapes and colors. Figure is taken from [10]

A combination of the normalized ELM losses being large due to low collisionality, and the pedestal stored energy also being large, means that ELMs in ITER will be powerful. If the collisionality trend holds, an ELM in ITER represents an energy expulsion of 22 MJ which causes unacceptable damage to the plasma facing components. Different methods predict ELMs to have a more acceptable 5-11 MJ energy loss [10].

Another effect of having low collisionality is that the bootstrap current is increased [27]. As such, collisionality is an important factor deciding whether a plasma is ballooning or peeling limited, with low collisionality meaning that a plasma is more likely to be peeling limited, see **Sec. 1.6**. The low collisionality in ITER means that it is expected to operate at the peeling limit as opposed to most current experiments that are ballooning-limited. Since peeling and

ballooning ELMs are expected to behave differently. Therefore, an effort has been devoted to reach the peeling limit in European machines. The peeling limit has been achieved in the Swiss tokamak TCV in 2022 [24] and recently in JET, 2024 [28].

1.8 Thesis objective

This work is part of the experiment conducted in JET where a peeling limited pedestal was successfully created. The goal of the experiment is a comprehensive comparison of the pedestals behaviour at the peeling and ballooning limits. Through this, the experiment ultimately aims to improve predictions on the behaviour of ITERs pedestal [29].

The objective of this thesis is to analyse how energy losses from ELMs at the peeling limit depend on different parameters. Especially important is whether the peeling limited ELMs are consistent with the energy loss trend in collisionality apparent in **Fig. 9**.

2 Theory

2.1 Parameters

The plasma in a tokamak can be described by parameters that are divided into two categories, plasma parameters and engineering parameters.

Plasma parameters describe properties and behaviour of the plasma. These are typically what is most closely related to the performance of the plasma. Engineering parameters describes how the plasma is being operated. These can be changed in order to change the plasma parameters and properties of the plasma. Some plasma parameters that are relevant for this work are listed below.

- **Temperature** can refer to the ion temperature or the electron temperature. Typically these are similar as ions and electrons interact and exchange kinetic energy frequently, they are however not necessarily identical. In this, work mainly the electron temperature is treated. It is worth noting that temperature is typically given in units of electronvolt and $1\text{eV} = k_{\text{B}}\text{K}$ where $k_{\text{B}} = 8.617 \cdot 10^{-5}\text{eV K}^{-1}$ is the Boltzmann constant.
- **Density** can similarly be divided into electron density and ion density. Any local difference in density between electrons and ions would lead to an electromagnetic force that would cancel out the difference. This ensures quasi-neutrality for the plasma and means there is no great difference in the density of electrons and ions. Density, in this work, refers to number density and has unit m^{-3} .
- **Pedestal temperature** is the temperature at the top of the pressure pedestal. This is calculated as the temperature at the inner boundary of the edge region.

- **Pedestal density** is the density at the pedestal of the pressure profile. This is calculated as the density at the same coordinate as the pedestal temperature.
- **Pedestal stored energy** is the energy gained by having a pedestal. It is used to normalize the energy losses for ELMs. For how the pedestal stored energy is calculated, see **Sec. 3.5**.
- **Normalized Plasma β** is the ratio of the plasma pressure and the magnetic field pressure. It is defined as,

$$\beta = \frac{\langle p \rangle}{B^2/(2\mu_0)}, \quad (8)$$

where B is the magnetic field strength, μ_0 is the vacuum permittivity and $\langle p \rangle$ is the average pressure. For this work the normalized β_N is relevant. It is defined as,

$$\beta_N = \beta \frac{aB_T}{I_p}, \quad (9)$$

where a is the minor radius of the plasma cross-section, B_T is the magnetic field in the toroidal direction and I_p is the plasma current [30].

Engineering parameters that are relevant for this work are briefly described below.

- **Power** describes how much energy is being added to the plasma. JET is mainly heated through neutral beam injection (NBI) where neutral particles are accelerated to high energies before being shot into the plasma where they will interact with particles, transferring energy to the plasma. The plasma can also be heated through Ion Cyclotron Resonance Heating (ICRH). ICRH works by sending photons with the same frequency as the ions rotate around the magnetic field lines. This makes them likely to be absorbed by the ions. The ions in turn interact with other particles, spreading the heat through the plasma.
- **Magnetic field strength** describes how strong the toroidal magnetic field that confines the plasma is.
- **Gas rate** describes the rate at which gas which fuels the plasma is being supplied to the plasma. Gas rate is mostly believed to affect the density of the plasma. However, an increase in gas rate can lead to more frequent ELMs and thus lower the density rather than increase it.
- **Effective mass** serves as a measurement of the ratio between deuterium and tritium. It is measured as,

$$A_{\text{eff}} = C_H u + C_D 2u + C_T 3u. \quad (10)$$

Here, C_H , C_D and C_T represent the concentrations of hydrogen, deuterium and tritium supplied to the plasma. The concentrations take into account both fuel gas and particles injected through the neutral beam injector. As such, if the plasma is supplied mostly with deuterium, A_{eff} is closer to two. If the plasma is mainly supplied with tritium, A_{eff} is closer to three.

2.2 Diagnostics

This work is based on measurements of electron temperature and density using three types of diagnostic systems, Thomson Scattering (TS), Reflectometry and Electron Cyclotron Emission (ECE). Additionally, a measurement of the total energy of the plasma is found through the diamagnetic signal and a measurement of the density of the plasma is found through interferometry. Lastly, the beryllium recombination spikes whenever particles are ejected from the plasma. These diagnostics and the principle of how they work are briefly presented here.

2.2.1 Thomson scattering

Thomson Scattering works by shooting a laser beam at the plasma and allowing it to scatter off the free electrons in the plasma. The power scattered is proportional to the density of the plasma and the temperature of the plasma is related to the broadening of the scattered spectrum [14]. Since TS measures temperature and density simultaneously it can be used to ensure that the other measurements are mapped correctly to the flux coordinate allowing for a full profile of the density and temperature for all values of the flux coordinate.

A problem with JETs TS diagnostic is that it operates with a frequency of 20 Hz, yielding measurements every 50 ms. To compensate for this poor time resolution, other diagnostics are necessary to get information of the density and temperature profiles both before and after the ELMs. The diagnostic that measures Thomson scattering in JET, that has been used in this work, is called High Resolution Thomson Scattering (HRTS).

2.2.2 Reflectometry

Reflectometry works by shooting beams of microwave radiation towards the plasma. The radiowaves are reflected off the plasma at a critical density depending on the frequency of the microwaves according to,

$$\omega = \left(\frac{n_e e^2}{\epsilon_0 m_e} \right)^{1/2}. \quad (11)$$

Where n_e is the electron density at a certain spatial coordinate, e is the electron charge, ϵ_0 is the vacuum permittivity and m_e is the electron mass. The travel time of the light is then measured to determine the physical location of the critical density [14]. By sending different frequencies of radiowaves the density profile of the plasma can be found.

JETs reflectometry operates with a frequency of 2 kHz, yielding measurements every 0.5 ms. This time resolution allows its use even in narrow time windows. The diagnostic that measures reflectometry in JET and that has been used for this work, is called KG10. KG10 generates a lot of data with a large spread in ψ . This spread makes it difficult to fit a curve to the data. As such, an average of all included data is formed for each different frequency at which measurements are made. The averages have very little spread in ψ and so a profile can be fitted to them. This process is referred to as rebinning.

2.2.3 Electron cyclotron emission

Electron cyclotron emission (ECE) is the radiation emitted when an electron gyrates around a magnetic field line. The frequency of this radiation is proportional to the magnetic field strength and so the magnetic field strength is known for where the radiation was emitted. The radiation then has to travel through the plasma which will interfere with the signal. When the plasma can be considered optically thick the intensity will follow Rayleigh-Jeans law [14],

$$I_n(\omega) = \frac{\omega^2 T_e(R)}{8\pi^3 c^2}. \quad (12)$$

By measuring the intensity the temperature is thus determined.

JETS ECE diagnostic operates with a frequency of 2.5 kHz, yielding measurements every 0.4 ms. This time resolution guarantees measurements in narrow time intervals. A disadvantage is that it relies on the plasma being optically thick and therefore the results are unreliable at the edge of the plasma. The diagnostic that measures ECE that has been used for this work is called KK3.

2.2.4 Diamagnetic energy

By placing a loop poloidally around the plasma the magnetic flux can be measured. By comparing the flux with plasma and the flux without plasma the diamagnetic flux can be found. The diamagnetic flux can be related to the total energy stored in the plasma [14]. This is both used to calculate the energy drop from an ELM and in order to select ELMs. A disadvantage with this method is that the signal is very noisy. The energy measurement using diamagnetic flux is referred to as W_{dia} .

2.2.5 Interferometry

Interferometry works by shooting a laser at the plasma with a frequency that is high compared to the frequency of the plasma. Coming out of the plasma the laser will have a phase delay according to [14],

$$\Delta\phi = \left(\frac{\lambda e^2}{4\pi\epsilon_0 m_e c^2} \right) \int n_e dl. \quad (13)$$

The phase shift can be measured as an interference with an undisturbed laser that does not go through the plasma. Using the measured phase shift the line integrated density can be deduced. Since the density drops after an ELM this signal can be used to find ELMs. The diagnostic measuring the line integrated density through interferometry, that has been used for this work, is called LID4.

2.2.6 Beryllium recombination line emission

Whenever an ELM causes particles to be ejected from the plasma these will interact with the plasma facing components. In JET the plasma facing wall

consists of beryllium. When it interacts with emitted particles electrons will be knocked free from the beryllium atoms and other electrons will recombine with the beryllium. The recombination emits a photon at a precise frequency and therefore, a spike in this frequency usually coincides with ELMs. This diagnostic is the primary tool used for ELM selection. The diagnostic that measures the beryllium recombination line emission, that has been used for this work is called TBEL.

3 Method

The energy losses of ELMs have been estimated using two different methods that rely on different diagnostics. The first method relies on temperature and density profiles in the plasma. These are recreated using data from ECE, reflectometry and TS diagnostics described in **Sec 2.2.1 - 2.2.3**. Comparing the profiles before and after an ELM gives the energy loss. Energy losses calculated using this method are referred to as ΔW_{prof} . The second method calculates the energy loss by comparing the W_{dia} signal before and after the ELM. Energy losses calculated using this method are referred to as ΔW_{dia} . This section describes how ELMs are identified, different methods used to calculate ELM energy losses and operational parameters of the data set on which this work is based.

3.1 ELM selection

Stationary time intervals—that is, intervals where parameters such as stored energy and density are close to constant—are chosen for investigation. Each interval represents one data point in **Sec. 4**, regardless of how many ELMs it contains. For each interval, the data for the different ELMs is used together. To do so, it is assumed that all ELMs inside each interval have similar characteristics. This is justified as long as important parameters such as density and stored energy are constant enough through the interval. Typically, a time interval lasts around 0.5s and contains somewhere between 3-10.

For each of these intervals, W_{dia} , the beryllium recombination signal and the line integrated density are plotted as is exemplified by **Fig. 10**. Anywhere there is a drop in W_{dia} and line integrated density, combined with a spike in beryllium recombination, is marked as an ELM.

3.2 Profile fitting

Firstly, all the data from TS, ECE, and reflectometry from right before an ELM—marked with green in **Fig. 10**—is grouped together. This data serves to create profiles of the plasma temperature and density. These profiles are referred to as pre-ELM profiles. The same process is repeated with data from right after an ELM, marked by yellow in **Fig. 10**. These profiles are referred to as post-ELM profiles. Typically, the time window from which data is taken for the pre-ELM profile is between 5 and 1ms before the ELM. The time window

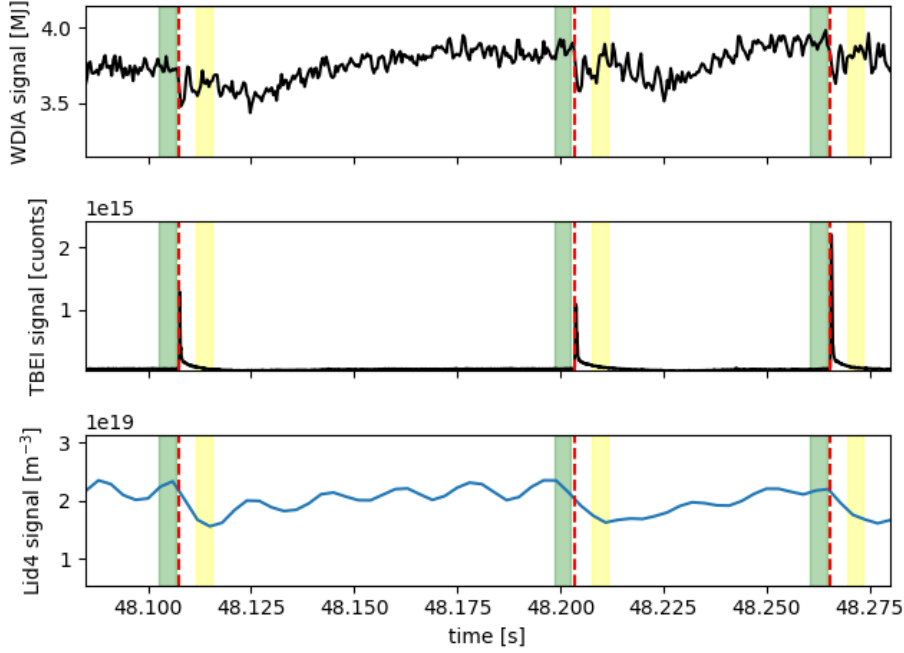


Figure 10: The signal of diagnostics that are important for ELM selection. The first plot shows the diamagnetic measurement of the plasma stored energy. The second plot shows the beryllium recombination. The third plot shows the line integrated density. Yellow and green fields represent the time windows where data has been taken to create pre- and post-ELM profiles respectively. The data comes from shot 103705.

used for the post-ELM is typically between 4 and 8ms after the ELM. Data too close to ELMs are avoided as diagnostics tend to be more unreliable. The exact time windows vary as the characteristics of the ELMs vary.

The used TS diagnostic produces data too seldom—see **Sec. 2.2.1**—for it to reliably yield at least one data set reasonably close to before and after an ELM for each interval. As such, it is not used to create the final fits. It still plays an important role in making sure the ECE and reflectometry measurements are correctly mapped to the flux coordinate. This is done by first shifting the TS data in ψ so that its fitted curve has temperature 100 eV at the separatrix in the pre-ELM profile. All TS measurements yield both a temperature and density values. Thus, shifting the temperature TS values also shifts the corresponding TS density values. The reflectometry and ECE data is then shifted so that it aligns with the TS density and temperature measurements respectively. The same shifts are applied for all ELMs in an interval, pre- and post-ELM. Shifts are justified because errors in mapping the diagnostics are significant compared

to the temperature at the separatrix, which is instead used for alignment. Shifts only move data in ψ direction.

Fig. 11 shows fitted temperature and density profiles along with the data to which it is fitted. For the temperature profiles, a modified hyperbolic tangent is used to describe the outer parts of the plasma. It is similar to a hyperbolic tangent except that it contains an additional parameter, s , which allows for a slope inside of the pedestal. It can mathematically be described as,

$$T(\psi) = \frac{h}{2} \left(\frac{(1 + sx)e^x - e^{-x}}{e^x + e^{-x} + 1} \right), \quad (14)$$

where,

$$x = \frac{2(\psi_{\text{ped}} - \psi)}{\Delta} \quad (15)$$

In this expression, h is the height of the pedestal and gives the temperature value right inside of the pedestal. ψ_{ped} is the position of the pedestal and it is defined as the position where the derivative of the temperature with respect to ψ , has the highest value. Δ is the width of the pedestal region with increased gradient. $\Delta, \psi_{\text{ped}}, h$ and s are parameters that are optimized to fit the data. The same function is used to fit the post-ELM temperature profile.

Similar fits are created for the density profile except that two additional degrees of freedom are included to allow for an offset h_2 and an incline, s_2 outside of the pedestal. The fitted function can be described by,

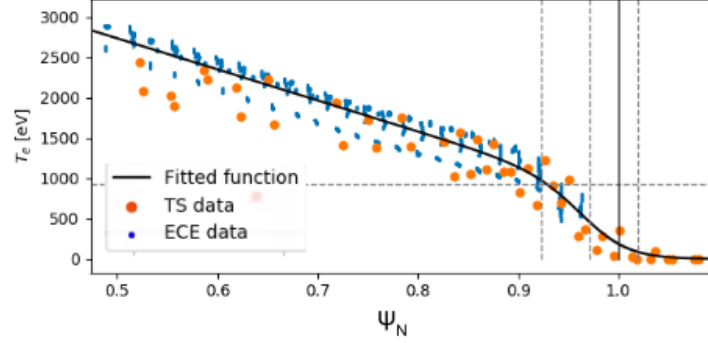
$$p(\psi) = \frac{h}{2} \left(\frac{(1 + sx)e^x - (1 + s_2x)e^{-x}}{e^x + e^{-x} + 1} \right) + h_2, \quad (16)$$

where x is the same as described in 15. The parameters that are optimized for this fitted function are $\Delta, \psi_{\text{ped}}, h, s, h_2$ and s_2 .

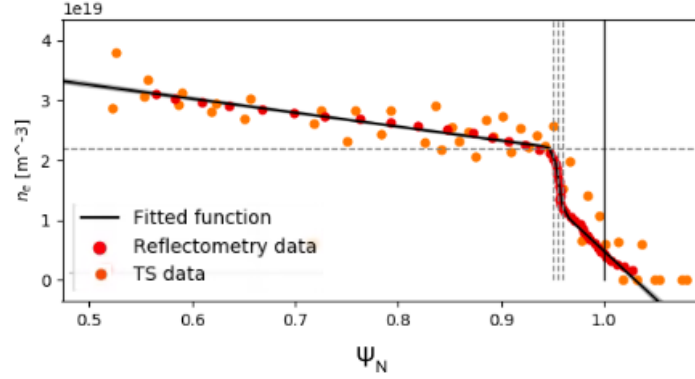
3.3 Energy loss from profiles

By comparing the pre- and post-ELM profiles shown in **Fig. 12a** and **Fig. 12b**, losses in temperature and density can be calculated. The local temperature and density losses are shown in **Fig. 12c** and **Fig. 12d**.

The energy losses can be divided into convective and conductive energy losses. Dividing the energy losses this way allows for a more detailed description of the ELM and could yield interesting results. The convective energy losses comes from particles leaving the plasma, while the conductive energy losses comes from the plasma losing temperature. The total energy loss is nearly the sum of the conductive and convective energy loss. A correctional cross-term should be subtracted but it is negligible. The energy losses and the cross-term can be calculated using **Eq. 17- 19** where the factor $\frac{dV}{d\psi}$ converts volume coordinates to the coordinate system described in **Sec. 1.4**. The total energy loss is $\Delta W_{\text{Tot}} = \Delta W_{\text{conductive}} + \Delta W_{\text{convective}} - \Delta W_{\text{cross-term}}$ [22].



(a)



(b)

Figure 11: **Fig. 11b** shows temperature measurements and a fitted modified tangent hyperbolic function. **Fig. 11a** shows density measurements along with a fitted function. The fitted function is a modified tangent hyperbolic that is allowed to have an incline and an offset from zero for the region outside of the pedestal. Note that the TS data has not been used for either fit. The data comes from pre-ELM windows from shot 103894 between 47.04-47.52s.

$$\Delta W_{\text{conductive}} = \frac{3}{2}k \int \Delta T n dV = \frac{3}{2}k \int \Delta T n \frac{dV}{d\psi} d\psi \quad (17)$$

$$\Delta W_{\text{convective}} = \frac{3}{2}k \int T \Delta n dV = \frac{3}{2}k \int T \Delta n \frac{dV}{d\psi} d\psi \quad (18)$$

$$\Delta W_{\text{cross-term}} = \frac{3}{2}k \int \Delta T \Delta n dV = \frac{3}{2}k \int \Delta T \Delta n \frac{dV}{d\psi} d\psi \quad (19)$$

In **Eq. 17 - 19** any quantity with Δ in front of it refers to the difference in the quantity between the pre- and post-ELM profiles. Any other quantity refers to the value before an ELM. k refers to the Boltzmann constant. The integrals

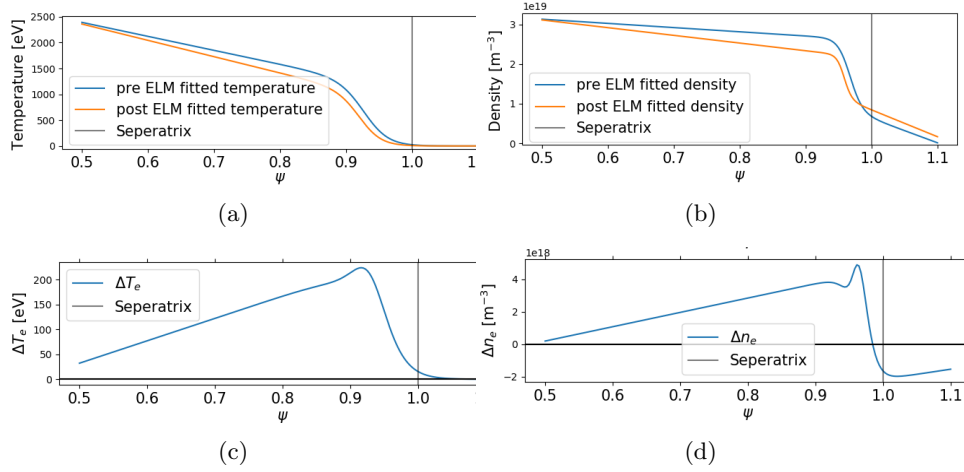


Figure 12: **Fig. 12a** and **12b** shows density and temperature profiles respectively. **Fig. 12c** and **Fig. 12d** show the corresponding losses in temperature and density respectively. The fits are created using data before and after ELMs in the time window 49.18-49.68 from shot 102072.

are only done in the interval between $\psi = 0.75$ and $\psi = 0.99$ as this is where the main losses are found. Additionally, the integrals are no longer well-defined for $\psi \geq 1.0$ as the flux surfaces no longer have a finite surface area and $\frac{dV}{d\psi}$ is no longer defined.

To get the total energy the ion energy and the electron energy should be added together. For this work only measurements of the electrons temperature and density are used and as such only the electron energy has been included.

The uncertainty of the energy measurements comes from uncertainty in the pressure which in turn comes from uncertainty in temperature and density. An estimate of the variance of temperature and density is found by investigating the spread in data between $\psi_{\text{ped}} - 0.1$ and ψ_{ped} . Here ψ_{ped} is the pedestal position in the fitted temperature function.

The variance of the temperature data is estimated as,

$$\text{Var}(T) = \frac{\sum_{i=1}^N (T(\psi_i) - T_i)^2}{N}. \quad (20)$$

Where $T(\psi_i)$ is the temperature according to the fitted function described in **Eq.14**, T_i is the measured temperature for data point i and N is the total amount of data points in the interval. The variance of the density is similarly estimated using **Eq. 21**. The density variance is calculated using reflectometry data without rebinning, since the removes almost all the uncertainty incorrectly.

$$\text{Var}(n) = \frac{\sum_{i=1}^N (n(\psi_i) - n_i)^2}{N} \quad (21)$$

Using the variance of the temperature and the density, an estimate of the pressure is calculated as,

$$\text{Var}(p) = \text{Var}(T) \left(\frac{\partial p}{\partial T} \right)^2 + \text{Var}(n) \left(\frac{\partial p}{\partial n} \right)^2. \quad (22)$$

Since the energy is the integrated pressure, the uncertainty in energy should be proportional to the uncertainty in pressure. Using this, the variance in energy can be approximately related to the variance in pressure at the pedestal according to **Eq. 23**.

$$\frac{\text{Var}(p_{\text{ped}})}{p_{\text{ped}}^2} \approx \frac{\text{Var}(\Delta W_{\text{prof}})}{(\Delta W)^2} \quad (23)$$

Finally, the uncertainty in energy is calculated as,

$$\sigma_{\Delta W_{\text{prof}}} = \sqrt{\text{Var}(p) \frac{(\Delta W)^2}{p_{\text{ped}}^2}}. \quad (24)$$

3.4 Energy loss from W_{dia}

The energy losses are calculated in two ways using W_{dia} . The first method calculates the energy drop for each individual ELM by comparing pre- and post-ELM energy levels. The pre- and post-ELM energy levels are calculated as the average of the W_{dia} signal in a time window before and after an ELM respectively. Typically, the pre- and post-ELM time windows are roughly 7 to 1ms before an ELM and 1 to 5ms after an ELM respectively. An example of the pre-ELM time window is shown in green in **Fig. 13**, the post-ELM time window is shown in yellow. Since a value for the energy loss is generated for each ELM, the uncertainty for an interval can be calculated as the standard deviation of these values. This method is referred to as the average windows method.

The second method uses moving averages. For a given time point, the moving average is calculated as the average of all data points within a specified time range around that point. This allows the signal to be smoother and more resilient to the influence of noise. By looking at the moving average in a region around the ELM, the pre- and post-ELM energy levels are chosen manually. An example of how the energy levels are marked using this method is shown in **Fig. 14** where the pre- and post-ELM energy levels are highlighted.

For each time point with a moving average an uncertainty can be calculated using the same data. As such, the value chosen as the pre-ELM average has a variance $\text{Var}(W_{\text{dia}}^{\text{pre}})$ and the post-ELM average has variance, $\text{Var}(W_{\text{dia}}^{\text{post}})$. The uncertainty of the energy loss is calculated using **Eq.25**.

$$\sigma_{\Delta W_{\text{dia}}} = \sqrt{\text{Var}(W_{\text{dia}}^{\text{pre}}) + \text{Var}(W_{\text{dia}}^{\text{post}})}. \quad (25)$$

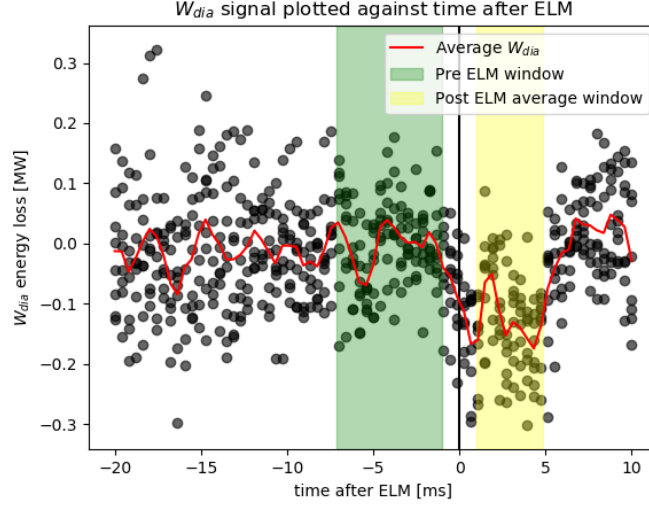


Figure 13: All diamagnetic measurements of the plasma stored energy in a period between 20ms before an ELM to 10 ms after an ELM plotted in the same figure. To ensure that all profiles are comparable the pre-ELM average energy has been subtracted from the whole signal. Data is taken from 1030708 between 48.24 s and 48.75 s

3.5 Pedestal stored energy and normalization

In certain contexts it is better to have the ELM energy loss normalized to remove dependency on how much energy is stored in the plasma. Normalized ELMs are especially useful as they can be compared to other ELMs even if they are not part of the same experiment or even come from the same device. This is typically done by dividing the energy loss by the pedestal stored energy. Pedestal stored energy is the increase in energy stored in the plasma due to it having a pedestal. In **Fig. 15** an example of the elevating effect of the pedestal on the pressure profile is highlighted. Integration of the pedestal pressure according to **Eq. 26** gives the pedestal stored energy.

$$W_{\text{ped}} = \frac{3}{2}k \left(\int_0^{\psi_{\text{ped}}} n_{\text{ped}} T_{\text{ped}} \frac{dV}{d\psi} d\psi + \int_{\psi_{\text{ped}}}^1 T(\psi) n(\psi) \frac{dV}{d\psi} d\psi \right). \quad (26)$$

Here, ψ_{ped} is the flux coordinate at the inner boundary of the pedestal region. n_{ped} and T_{ped} is the density and temperature respectively at the pedestal coordinate. Lastly, k is the Boltzmann constant.

Since the diamagnetic signal does not give any information on where the energy is stored it can not be used to calculate the pedestal stored energy. As such, the same method is used to normalize the energy loss calculated from the

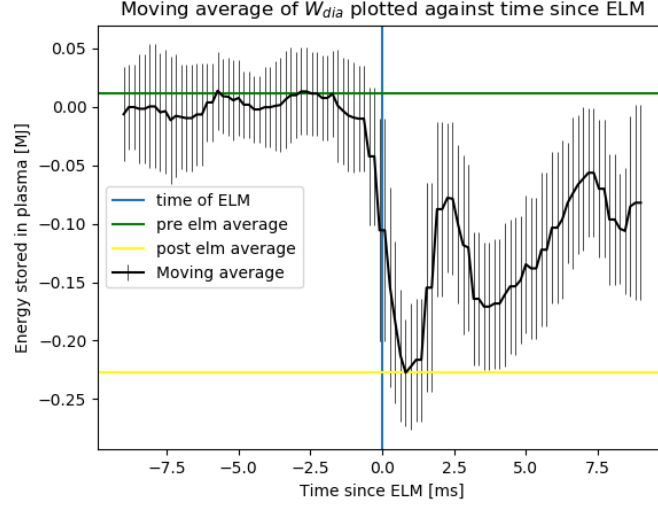


Figure 14: The moving average of the diamagnetic measurement of the plasma stored energy using a window of 2 ms. The energy loss is calculated as the difference between the pre-ELM average and the post-ELM average. Data is taken from shot 103705 between 48.07 and 48.46 seconds.

diamagnetic signal. To account for the ion energy being included in diamagnetic signal, the energy loss is divided by an additional factor of two.

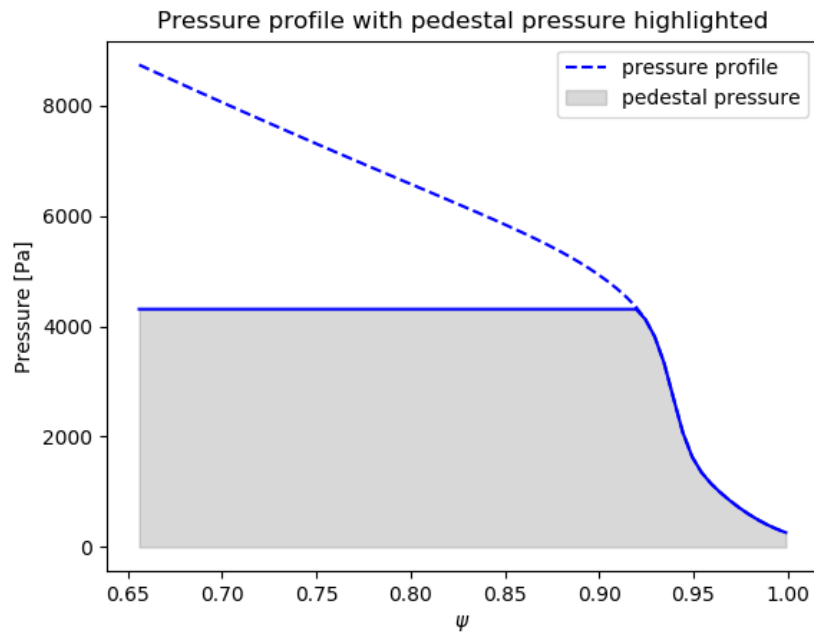


Figure 15: An example of a pressure profile where the pedestal pressure is highlighted. The pedestal pressure is integrated to calculate the pedestal stored energy.

3.6 Data Set

The data on which this work is based comes from a set of experiments aimed at reaching peeling limited pedestals in JET. The dataset is characterized by a standard plasma current 1.4 MA and a highly triangular shape [28]. To reach the peeling boundary, the current has been kept while the toroidal magnetic field has been increased for each shot from 1.7 to 3.8 T. As a result, the safety factor increases from a standard value $q_{95} = 3.7$ to a high value $q_{95} = 8.2$. This is done because numerical simulations show that a safety factor of $q_{95} > 7.0$ is necessary to reach a peeling limited pedestal.

Experimental results show a peeling limited pedestal indeed has been achieved. For a more detailed discussion, see [28]. As an example, **Fig. 16** shows the peeling-ballooning stability diagram for the JET pulse 102752 at 1.4MA, 3.8T and 25MW. α is the normalized pressure gradient. The star marks the position of the experimental pedestal and the thick line the stability boundary. The numbers represent the toroidal number of the most unstable mode, n . The pedestal is near the peeling boundary and it is limited by $n = 1 - 5$ which are peeling modes. The simulations are done using the HELENA code for the equilibrium and linear the MHD MISHKA code for stability. Further details are explained in [28].

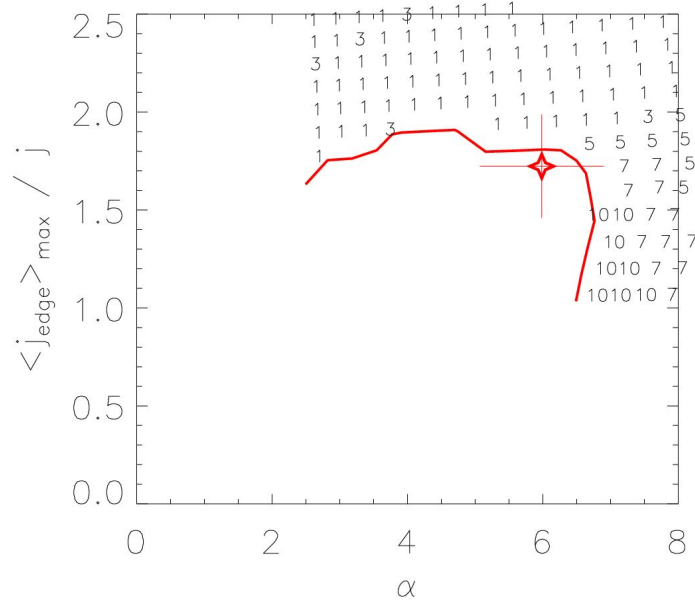


Figure 16: Stability region plotted in j - α space. As an example, the values for a shot from the experiment on which this work is based is highlighted by a red star. The numbers represent the most unstable modes. Figure is taken from [28] and depicts the stability of shot 102752.

The data on which this work is based is split into five data sets. These data sets are made to investigate how the size of ELMs change depending on certain parameters. The parameters are gas rate, density, magnetic field strength and effective mass. The data set investigating effective mass is further split in two, one where the NBI power is constant and one where β_N is constant. In order to investigate these dependencies other parameters have been kept as constant as possible and the desired parameter has been allowed to vary. Important operational parameters and information of the different time intervals in the different data sets are shown in **Tab. 1** - **Tab. 5**. Each shot represents a separate run of the plasma device. Note that some shots appear multiple times with different time windows. While all the listed parameters are similar within a shot, certain plasma parameters change, hence they are treated as separate data points.

| Shot | Time window [s] | I_p [MA] | B_T [T] | $A_{\text{eff}}[u]$ | NBI [MW] | ICRH [MW] | Gas[s ⁻¹] |
|--------|-----------------|------------|-----------|---------------------|----------|-----------|-----------------------|
| 103705 | 48.07-48.43 | 1.4 | 3.8 | 2.0 | 25 | 0.0 | $4 \cdot 10^{21}$ |
| 103705 | 48.49-48.74 | 1.4 | 3.8 | 2.0 | 25 | 0.0 | $4.0 \cdot 10^{21}$ |
| 103708 | 48.48-49.06 | 1.4 | 3.8 | 2.0 | 25 | 0.0 | $6.0 \cdot 10^{21}$ |
| 103708 | 47.68-48.00 | 1.4 | 3.8 | 2.0 | 25 | 0.0 | $6.0 \cdot 10^{21}$ |
| 103708 | 48.00-48.14 | 1.4 | 3.8 | 2.0 | 25 | 0.0 | $6.0 \cdot 10^{21}$ |
| 103800 | 48.08-48.94 | 1.4 | 3.8 | 2.0 | 25 | 0.0 | $4.0 \cdot 10^{21}$ |
| 103800 | 49.08-50.04 | 1.4 | 3.8 | 2.0 | 25 | 0.0 | $4.0 \cdot 10^{21}$ |
| 103800 | 50.09-50.65 | 1.4 | 3.8 | 2.0 | 25 | 0.0 | $4.0 \cdot 10^{21}$ |

Table 1: Operational parameters and important information for the gas scan data set.

| Shot | Time window [s] | I_p [MA] | B_T [T] | $A_{\text{eff}}[u]$ | NBI [MW] | ICRH [MW] | Gas[s ⁻¹] |
|--------|-----------------|------------|-----------|---------------------|----------|-----------|-----------------------|
| 103709 | 48.51-49.24 | 1.4 | 3.8 | 2.0 | 25 | 0 | $5 \cdot 10^{21}$ |
| 103708 | 48.64-49.30 | 1.4 | 3.8 | 2.0 | 25 | 0 | $6 \cdot 10^{21}$ |
| 104417 | 48.83-49.67 | 1.4 | 3.8 | 2.5 | 25 | 0 | $5 \cdot 10^{21}$ |
| 104281 | 49.18-50.47 | 1.4 | 3.8 | 2.8 | 25 | 0 | $5 \cdot 10^{21}$ |
| 104420 | 48.27-49.21 | 1.4 | 3.8 | 2.8 | 25 | 0 | $5 \cdot 10^{21}$ |

Table 2: Operational parameters and important information for the A_{eff} scan at constant P_{nbi} data set.

| Shot | Time window [s] | I_p [MA] | B_T [T] | $A_{\text{eff}}[u]$ | NBI [MW] | ICRH [MW] | Gas[s ⁻¹] |
|--------|-----------------|------------|-----------|---------------------|----------|-----------|-----------------------|
| 103709 | 47.70-47.90 | 1.4 | 3.8 | 2.0 | N/A | 0 | $5 \cdot 10^{21}$ |
| 103708 | 47.68-48.00 | 1.4 | 3.8 | 2.0 | N/A | 0 | $6 \cdot 10^{21}$ |
| 104417 | 47.13-47.31 | 1.4 | 3.8 | 2.5 | N/A | 0 | $5 \cdot 10^{21}$ |
| 104281 | 47.57-47.97 | 1.4 | 3.8 | 2.8 | N/A | 0 | $5 \cdot 10^{21}$ |

Table 3: Operational parameters and important information for the A_{eff} scan at constant β_N data set.

| Shot | Time window [s] | I_p [MA] | B_T [T] | $A_{\text{eff}}[u]$ | NBI [MW] | ICRH [MW] | Gas[s ⁻¹] |
|--------|-----------------|------------|-----------|---------------------|----------|-----------|-----------------------|
| 103481 | 45.13-45.56 | 1.4 | 1.7 | 2.0 | 25 | 0 | $8 \cdot 10^{21}$ |
| 103055 | 44.93-45.17 | 1.4 | 1.7 | 2.0 | 22 | 1 | $7 \cdot 10^{21}$ |
| 103057 | 45.63-46.01 | 1.4 | 2.2 | 2.0 | 22 | 1 | $7 \cdot 10^{21}$ |
| 103057 | 46.94-47.71 | 1.4 | 2.2 | 2.0 | 22 | 1 | $7 \cdot 10^{21}$ |
| 102081 | 45.78-46.20 | 1.4 | 2.8 | 2.0 | 21 | 3 | $6 \cdot 10^{21}$ |
| 102082 | 46.22-46.50 | 1.4 | 2.8 | 2.0 | 19 | 3 | $6 \cdot 10^{21}$ |
| 101861 | 47.45-47.98 | 1.4 | 3.1 | 2.0 | 21 | 3 | $8 \cdot 10^{21}$ |
| 103894 | 47.04-47.52 | 1.4 | 3.4 | 2.0 | 24 | 0 | $1.5 \cdot 10^{21}$ |
| 102068 | 48.50-48.94 | 1.4 | 3.4 | 2.0 | 21 | 3 | $7 \cdot 10^{21}$ |
| 102068 | 49.19-49.50 | 1.4 | 3.4 | 2.0 | 21 | 3 | $7 \cdot 10^{21}$ |
| 102069 | 48.56-48.95 | 1.4 | 3.4 | 2.0 | 21 | 3 | $7 \cdot 10^{21}$ |
| 102069 | 49.61-50.12 | 1.4 | 3.4 | 2.0 | 21 | 3 | $7 \cdot 10^{21}$ |
| 103705 | 48.07-48.43 | 1.4 | 3.8 | 2.0 | 25 | 0 | $4 \cdot 10^{21}$ |
| 103705 | 48.49-48.74 | 1.4 | 3.8 | 2.0 | 25 | 0 | $4 \cdot 10^{21}$ |
| 102238 | 47.19-47.43 | 1.4 | 3.8 | 2.0 | 22 | 3 | $7 \cdot 10^{21}$ |
| 102752 | 47.62-48.35 | 1.4 | 3.8 | 2.0 | 22 | 3 | $7 \cdot 10^{21}$ |
| 102754 | 47.61-48.14 | 1.4 | 3.8 | 2.0 | 22 | 3 | $7 \cdot 10^{21}$ |
| 102754 | 47.61-48.14 | 1.4 | 3.8 | 2.0 | 22 | 3 | $7 \cdot 10^{21}$ |

Table 4: Operational parameters and important information for the B_T scan data set.

| Shot | Time window [s] | I_p [MA] | B_T [T] | $A_{\text{eff}}[u]$ | NBI [MW] | ICRH [MW] | Gas[s ⁻¹] |
|--------|-----------------|------------|-----------|---------------------|----------|-----------|-----------------------|
| 102068 | 48.50-48.94 | 1.4 | 3.4 | 2.0 | 21 | 3 | $7 \cdot 10^{21}$ |
| 102068 | 49.19-49.50 | 1.4 | 3.4 | 2.0 | 21 | 3 | $7 \cdot 10^{21}$ |
| 102069 | 48.56-48.95 | 1.4 | 3.4 | 2.0 | 21 | 3 | $7 \cdot 10^{21}$ |
| 102069 | 49.61-50.12 | 1.4 | 3.4 | 2.0 | 21 | 3 | $7 \cdot 10^{21}$ |
| 102071 | 48.60-48.96 | 1.4 | 3.4 | 2.0 | 21 | 3 | $4 \cdot 10^{21}$ |
| 102071 | 49.15-49.75 | 1.4 | 3.4 | 2.0 | 21 | 3 | $4 \cdot 10^{21}$ |
| 102072 | 47.93-48.42 | 1.4 | 3.4 | 2.0 | 21 | 3 | $7 \cdot 10^{21}$ |
| 102072 | 49.18-49.68 | 1.4 | 3.4 | 2.0 | 21 | 3 | $7 \cdot 10^{21}$ |
| 102072 | 49.97-50.24 | 1.4 | 3.4 | 2.0 | 21 | 3 | $7 \cdot 10^{21}$ |
| 102074 | 48.79-49.53 | 1.4 | 3.4 | 2.0 | 21 | 3 | $4 \cdot 10^{21}$ |
| 102074 | 49.07-49.45 | 1.4 | 3.4 | 2.0 | 21 | 3 | $4 \cdot 10^{21}$ |
| 102076 | 49.58-50.07 | 1.4 | 3.4 | 2.0 | 21 | 3 | $3 \cdot 10^{21}$ |
| 102079 | 48.11-48.51 | 1.4 | 3.4 | 2.0 | 21 | 3 | $10 \cdot 10^{21}$ |
| 102079 | 49.77-50.24 | 1.4 | 3.4 | 2.0 | 21 | 3 | $10 \cdot 10^{21}$ |
| 102079 | 50.18-50.90 | 1.4 | 3.4 | 2.0 | 21 | 3 | $10 \cdot 10^{21}$ |

Table 5: Operational parameters and important information for the density scan data set.

4 Results

4.1 Comparison of moving averages and window averages

In order to compare the different methods that use the diamagnetic signal, their results are plotted against each other in **Fig. 17**. It is clear that the moving averages method systematically generates larger results. This is reflected in by the fraction $\frac{\Delta W_{\text{moving}}}{\Delta W_{\text{window}}} = 1.39 \pm 0.28$. The spread is large considering the methods measure the same signal.

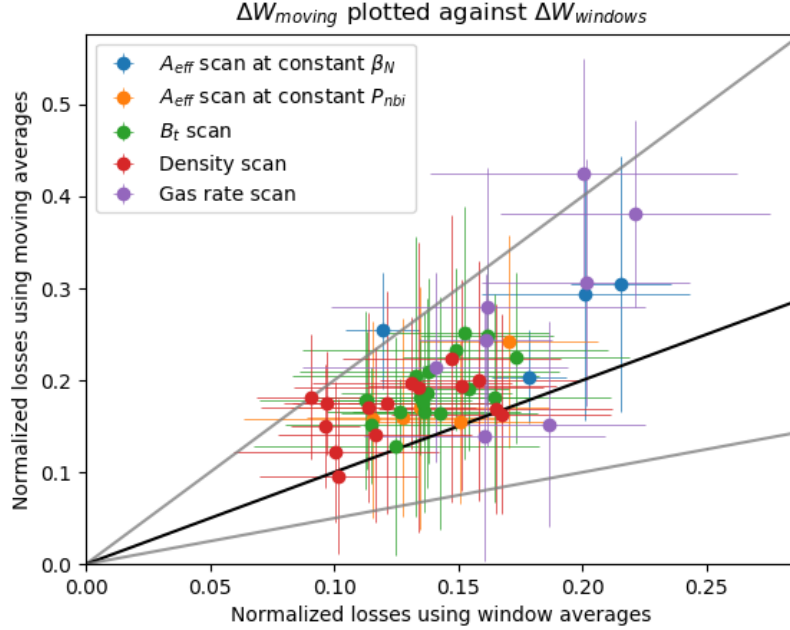


Figure 17: Energy losses calculated using the moving averages method plotted against the energy losses calculated using the window averages method. The black line represent the region where the results are equivalent. The gray lines represents the region where the results differ by a factor of two.

4.2 Comparison of diamagnetic measurements and profile fitting

To investigate the agreement between the two methods, ΔW_{dia} calculated using average windows is plotted against ΔW_{prof} in **Fig. 19**. Both the energy losses have been normalized as described in **Sec. 3.5**. The black line represents the region where $W_{\text{dia}} = 2W_{\text{prof}}$. Equivalently, for this line the normalized energies

are equal, $\Delta W_{\text{dia},N} = \Delta W_{\text{prof},N}$. If the ion and electron energy is the same the data points should be distributed along this line unless there is a systematic difference between the methods. Uncertainties in both measurements cause a spread of the data. Usage of ICRH is believed to worsen the performance of the two methods as it increases the frequency of ELMs and makes them irregular. Therefore, **Fig. 19b** excludes data points where ICRH has been used.

Using all data, it is found that $\frac{\Delta W_{\text{dia},N}}{\Delta W_{\text{prof},N}} = 1.11 \pm 0.42$. Using only the data without ICRH, it is found that $\frac{\Delta W_{\text{dia},N}}{\Delta W_{\text{prof},N}} = 1.12 \pm 0.25$. The two methods seem to agree average on. The uncertainty is smaller for the data that is not using ICRH. This implies that ICRH makes it more difficult to model the ELM losses for at least one of the methods.

The effect ICRH has on the plasma is most apparent in the beryllium recombination signal. The difference is showcased in **Fig. 18**. Despite both pulses having the same toroidal field strength, gas fueling rate the signals are very different. While **Fig. 18a** has regular well defined spikes, the shot with ICRH in **Fig. 18b** has more frequent irregular large spikes with lots of small spikes between them. This implies that the ELM-cycle is not as well-defined.

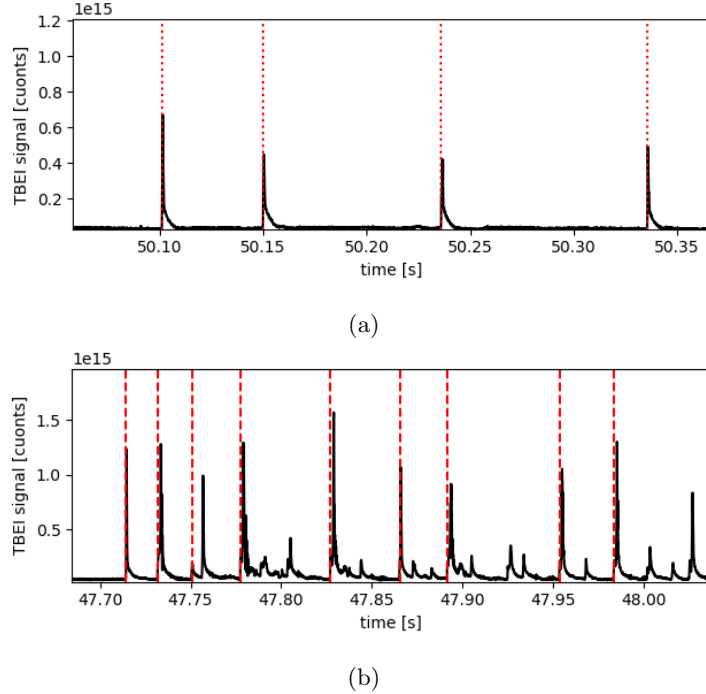


Figure 18: Two beryllium recombination signals are shown. The red dashed lines mark the time of ELMs. **Fig. 18a** shows data from shot 103800 where only NBI heating is used. **Fig. 18b** shows data from shot 102752.

In **Fig. 19a** there is a clear outlier that has higher ΔW_{prof} than the rest of the data points and comparatively low ΔW_{dia} . Excluding the outlier gives the value $\frac{\Delta W_{\text{dia},N}}{\Delta W_{\text{prof},N}} = 1.13 \pm 0.41$. The problematic data point is briefly discussed in **Sec. 6.1**. In **Fig. 20** ΔW_{dia} calculated using moving averages has been

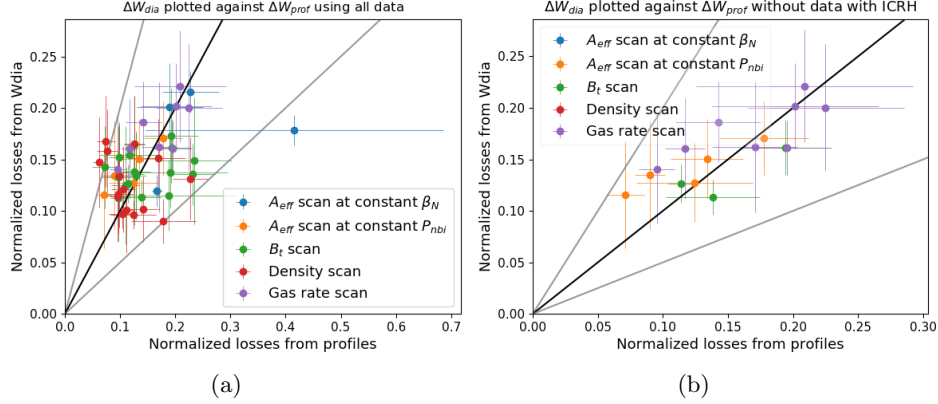


Figure 19: The normalized energy losses calculated with the WDIA-signal are plotted against the normalized energy losses calculated from the fitted profiles. The black lines show the region where the energy losses are equal. The gray lines show the region where the results differ by a factor of two. **Fig. 19a** includes all data points. **Fig. 19b** only includes data points without ICRH.

plotted against ΔW_{prof} . Using all data points gives $\frac{\Delta W_{\text{dia},N}}{\Delta W_{\text{prof},N}} = 1.52 \pm 0.56$. Using the same method but excluding data points where ICRH has been used gives $\frac{\Delta W_{\text{dia},N}}{\Delta W_{\text{prof},N}} = 1.54 \pm 0.36$. Since the agreement between the two signals is significantly worse and the uncertainty is larger, the method using moving averages has not been investigated further.

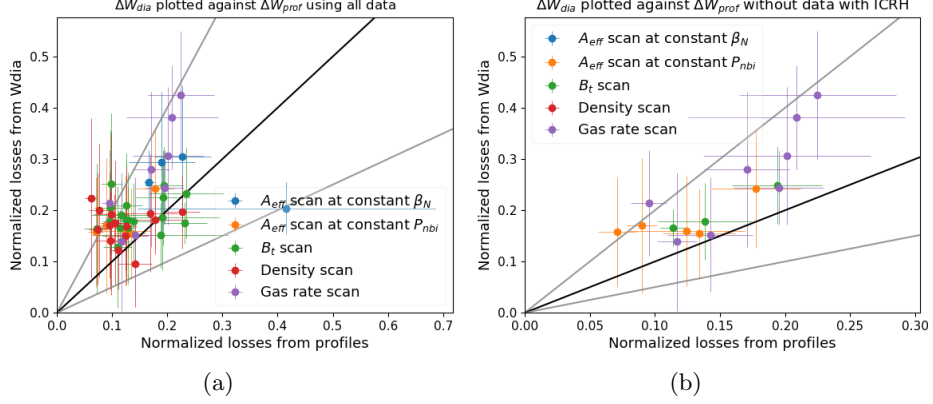


Figure 20: Normalized energy losses calculated with moving averages from the WDIA-signal plotted against normalized energy losses calculated from fitted profiles. The black lines shows the region where the energy losses are equal. The gray lines represent the region where the results differ by a factor of two. **Fig. 20a** includes all data points. **Fig. 20b** excludes data points with ICRH.

4.3 Comparison between convective and conductive losses

The profiles method calculates the conductive and convective energy losses separately. As such, trends in these can be investigated independently. The conductive energy losses are plotted against the convective energy losses in **Fig. 21**. As can be seen, two measurements roughly agree on average which is reflected by the value $\frac{\Delta W_{convective}}{\Delta W_{conductive}} = 0.96 \pm 0.41$. The spread is, however, quite large. The spread is mostly caused by some extreme outliers with low convective losses. Due to a lack of trends no further investigations using the conductive and convective energies are presented here.

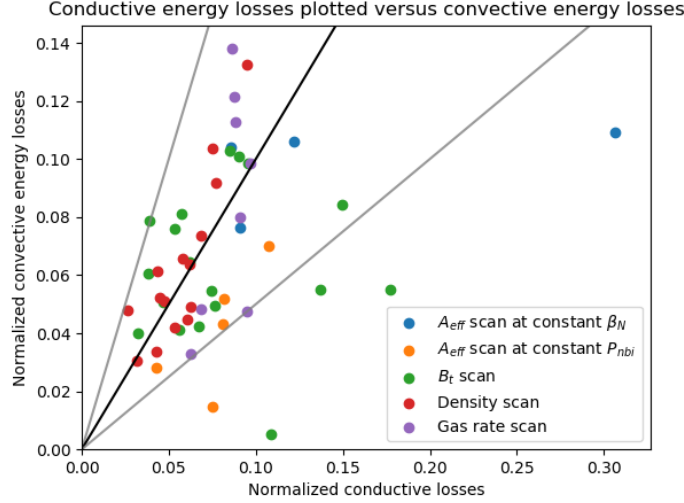


Figure 21: Normalized convective energy losses plotted against normalized conductive energy losses. The black line represents the region where $\Delta W_{\text{convective}} = \Delta W_{\text{conductive}}$. The gray lines represents the regions where they differ by a factor of two.

4.4 Dependencies on collisionality

Normalized energy is plotted against collisionality in **Fig. 22** to see if any trends are apparent. For each data point the collisionality is calculated as described in **Sec. 1.7**. For context, additional data from previous experiments is included and represented by the gray triangles. The reference data is taken from [10] and is compiled from multiple different machines in order to span a wide range of normalized collisionality.

Fig. 22a shows that $\Delta W_{\text{prof,N}}$ is in agreement with previous measurements. The previously mentioned outlier has a large value but also a large uncertainty. In **Fig. 22b** it can be seen that $W_{\text{dia,N}}$ also has values that are comparable to previous experiments.

Since ICRH is suspected to be a source of uncertainty the same plots are repeated while data points with ICRH are excluded in **Fig. 23**. Similarly to the plots using all data, there seems to be reasonable agreement between the energy losses calculated in this work and previous experiments.

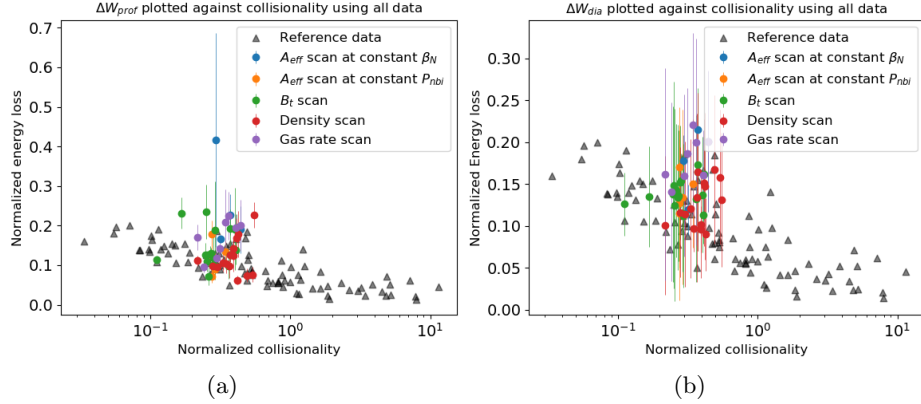


Figure 22: Normalized energy losses plotted against calculated collisionality. **Fig. 22a** uses energy losses calculated using fitted profiles. **Fig. 22b** uses energy losses calculated using WDIA signal. Reference data is taken from [10].

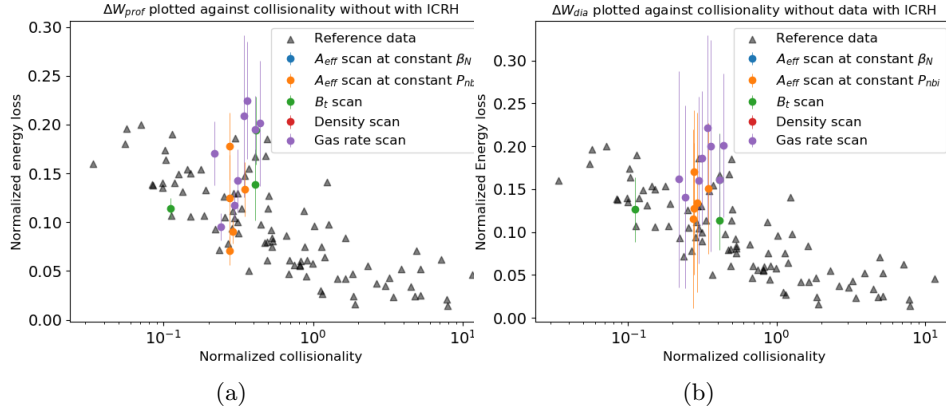


Figure 23: Normalized energy losses plotted against calculated collisionality. **Fig. 23a** uses energy losses calculated using fitted profiles. **Fig. 23b** uses energy losses calculated using W_{dia} signal. Data points where ICRH is used are excluded. Reference data is taken from [10].

4.5 Dependencies on magnetic field strength

In order to see if a trend can be found normalized energy losses are plotted against the toroidal magnetic field strength in **Fig. 24**. In order to avoid overlaps, a small artificial displacement has been added to the B_T values of certain data points. Only the data set investigating trends in the toroidal magnetic field strength, B_T , is included.

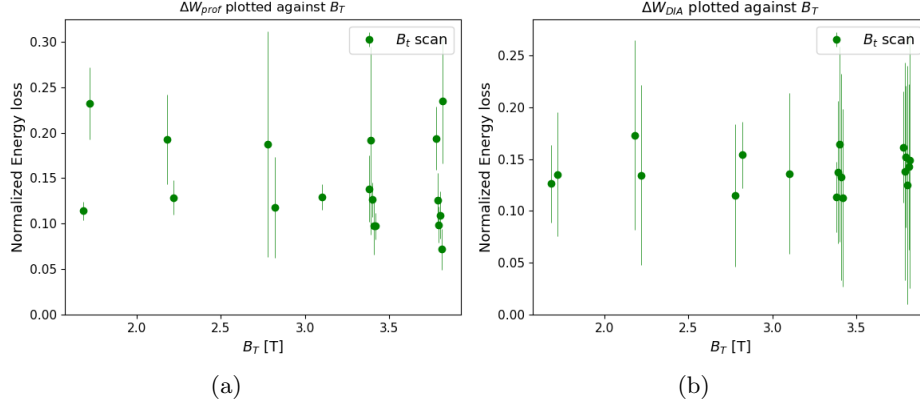


Figure 24: Normalized energy losses plotted against toroidal field strength, B_T . In **Fig. 24a** the energy losses are calculated using the fitted profiles. In **Fig. 24b** the energy losses calculated from the WDIA-signal is used. To avoid overlap certain data points have been given a slight displacement in B_T .

Similarly, the energy losses without normalization are plotted against the magnetic field strength in **Fig. 25**. Again, a slight displacement has been added to B_T to avoid overlapping data points.

The normalized and non-normalized plots are very similar, both for ΔW_{prof} and for ΔW_{dia} . No trend is apparent.

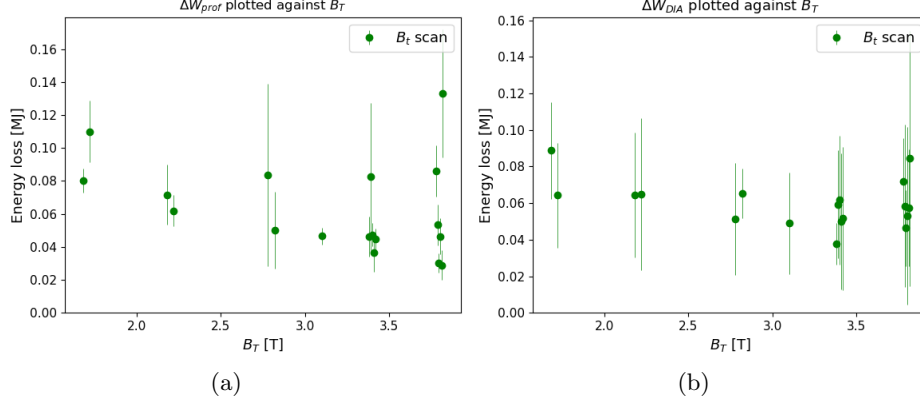


Figure 25: Energy losses plotted against toroidal field strength, B_T . In **Fig. 25a** the energy losses are calculated using the fitted profiles. In **Fig. 25b** the energy losses calculated from the WDIA-signal is used. To avoid overlap certain data points have been given a slight displacement in B_T .

4.6 Dependencies on density

In order to see if a trend can be found normalized energy losses are plotted against the pedestal density in **Fig. 26**. The pedestal density is chosen as it is representative of the density throughout the pedestal region. Only the data set investigating trends in the density is included.

Similarly, the energy losses without normalization are plotted against the pedestal density in **Fig. 27**.

The normalized and non-normalized plots are very similar, both for ΔW_{prof} and for ΔW_{dia} . No trend is apparent.

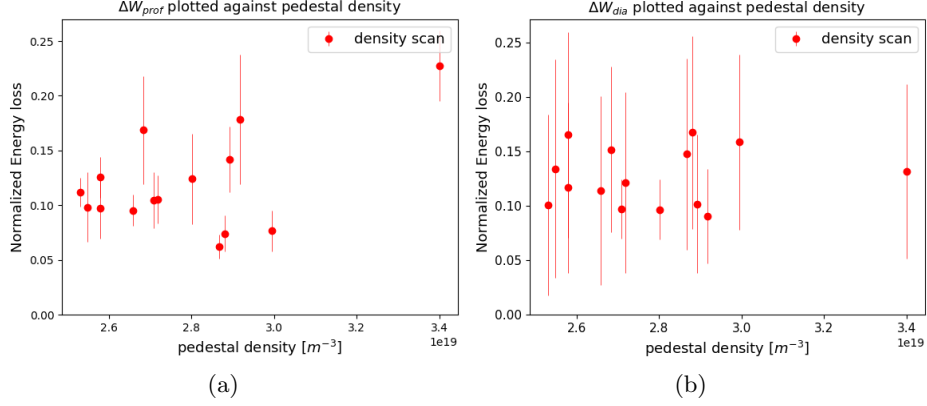


Figure 26: Normalized energy losses plotted against pedestal density. In **Fig. 26a** the energies are calculated using profiles. In **Fig. 26b** the WDIA-signal is used.

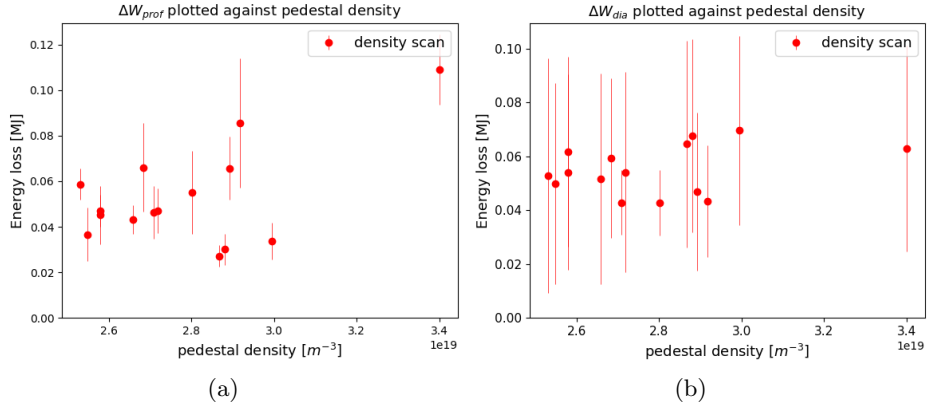


Figure 27: Energy losses plotted against pedestal density. In **Fig. 27a** the energies are calculated using profiles. In **Fig. 27b** the WDIA-signal is used.

4.7 Dependencies on gas fueling rate

The normalized energy losses are plotted against the gas fueling rate in **Fig. 28**. Only the data set investigating trends in the gas fueling rate is included.

For the same data set, energy losses without normalization are plotted against the gas fueling rate in **Fig. 29**. For both **Fig. 28** and **Fig. 29**, a slight displacement in gas fueling rate is added to avoid overlapping data points. The plots with normalized and non-normalized energy lost are very similar for both methods. There are no apparent trends.

The gas fueling rate is mostly expected to affect the density of the plasma.

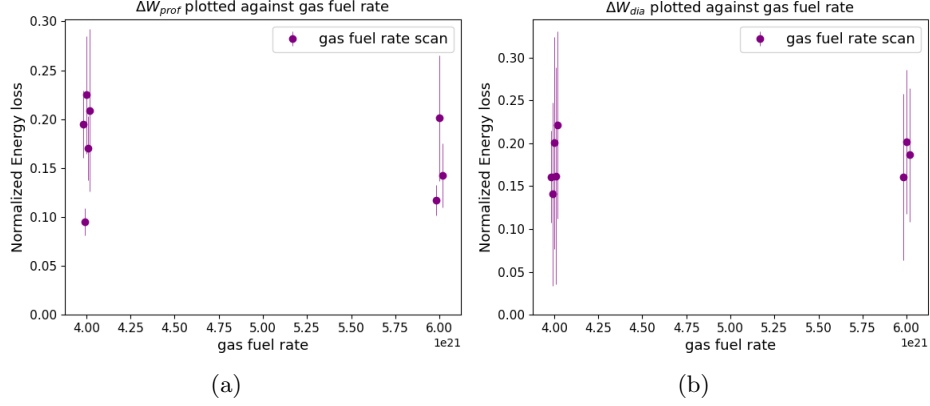


Figure 28: Normalized energy losses plotted against gas fueling rate. In **Fig. 28a** the energies are calculated using profiles. In **Fig. 28b** the WDIA-signal is used. A slight displacement in gas fueling rate is added to avoid overlapping data points.

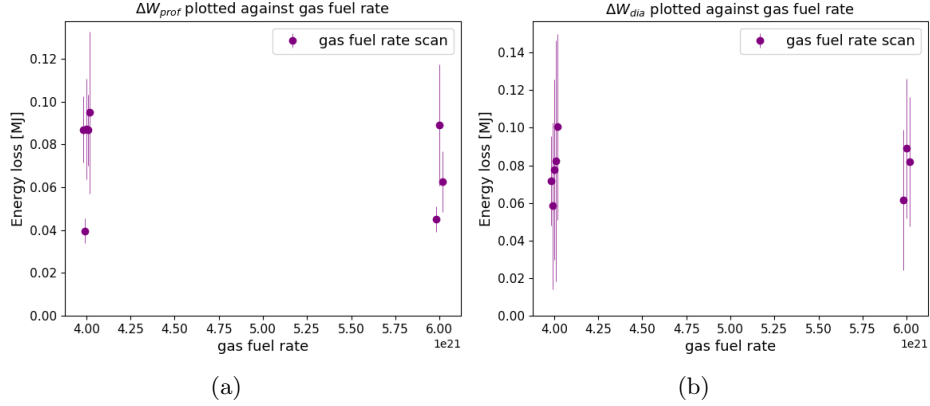


Figure 29: Energy losses plotted against gas fueling rate. In **Fig. 29a** the energies are calculated using profiles. In **Fig. 29b** the WDIA-signal is used. A slight displacement in gas fueling rate is added to avoid overlapping data points.

Therefore the normalized energy losses of the same data set is plotted against its pedestal density in **Fig. 30**. The energy losses without normalization are plotted against pedestal density in **Fig. 31**. The plots for normalized and non normalized energy losses are similar. No clear trends are apparent.

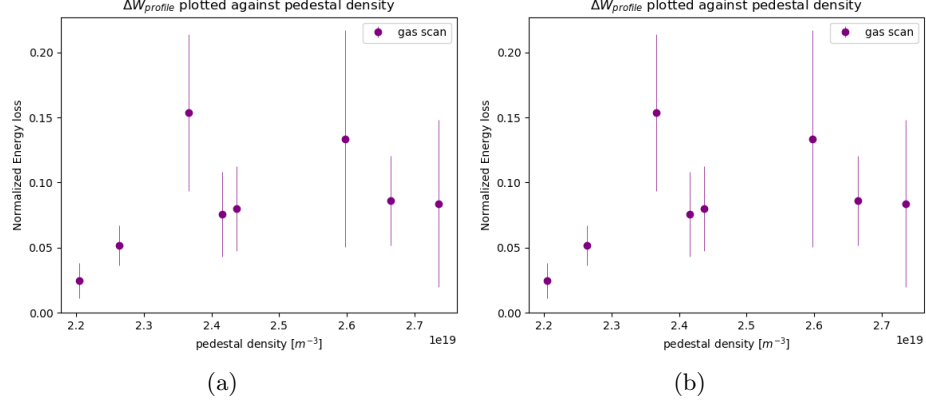


Figure 30: Normalized energy losses plotted against pedestal density. In **Fig. 30a** the energies are calculated using profiles. In **Fig. 30b** the WDIA-signal is used.

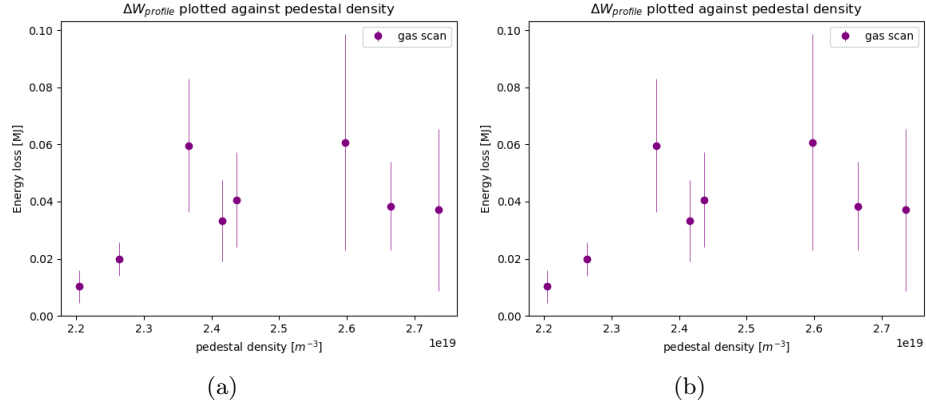


Figure 31: Energy losses plotted against pedestal density. In **Fig. 31a** the energies are calculated using profiles. In **Fig. 31b** the WDIA-signal is used.

4.8 Dependencies on effective area

In order to see if any trends can be found normalized energy losses are plotted against the effective mass. The data is split in two sets. For the first data set the plasma β_N was kept constant. For the second data set the power supply from the neutral beam injection is kept constant. The energy losses calculated from these data sets are shown in **Fig. 32** and **Fig. 33** respectively.

Fig 34 shows the energy losses without normalization plotted against the effective mass for the data set with constant plasma β_N . **Fig 35** shows the same but for the data set with constant power supply from neutral beam injection.

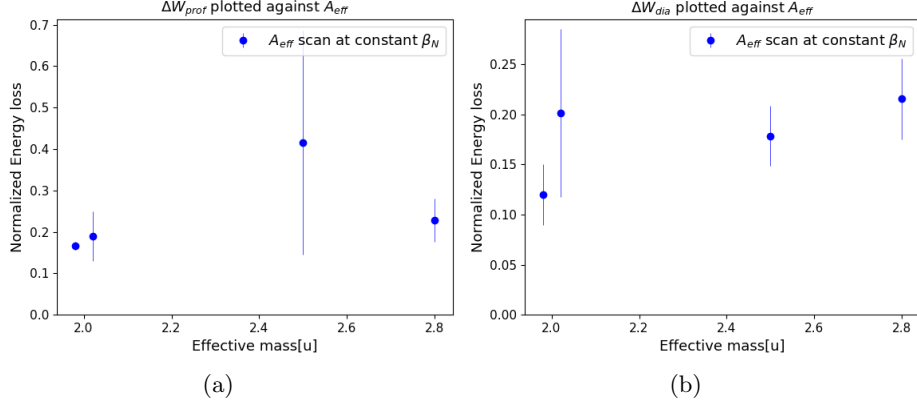


Figure 32: Normalized energy losses plotted against effective mass. In **Fig. 32a** the energy losses are calculated using the fitted profiles. In **Fig. 32b** the WDIA-signal is used. Only the data sets investigating trends in effective mass with constant plasma β_N are included.

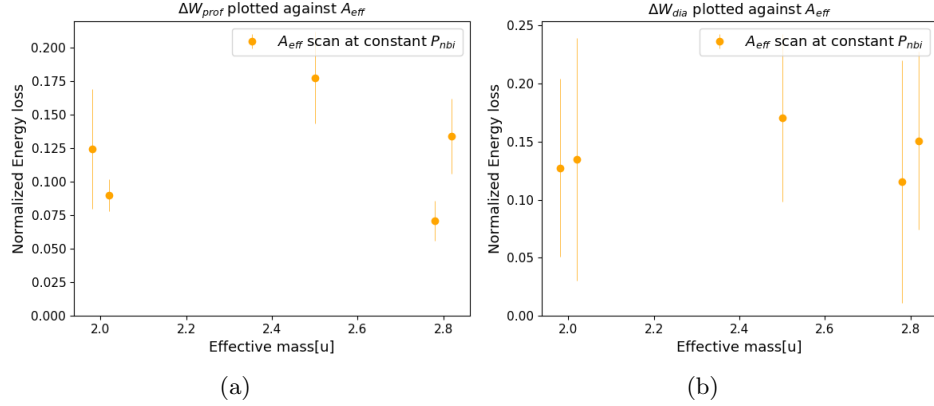


Figure 33: Normalized energy losses plotted against effective mass. In **Fig. 33a** the energy losses are calculated using the fitted profiles. In **Fig. 33b** the WDIA-signal is used. Only the data sets investigating trends in effective mass with constant power supply from neutral beam injection are included.

Neither the data set with constant β_N nor the data with constant P_{NBI} show any trend in A_{eff} .

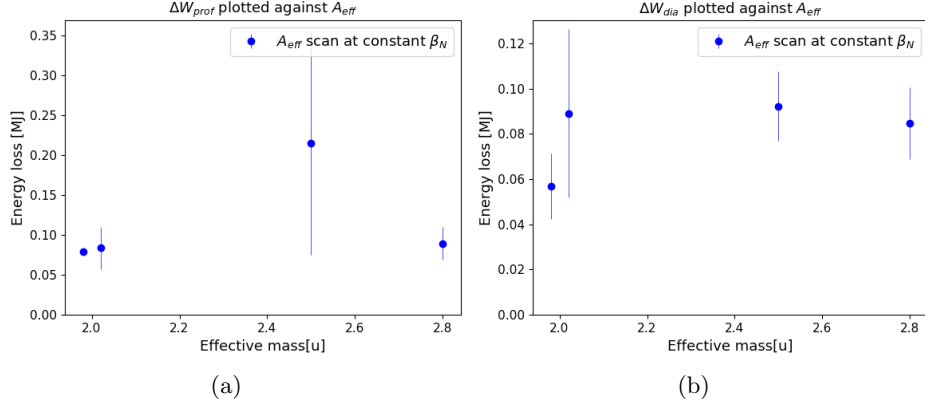


Figure 34: Energy losses plotted against effective mass. In **Fig. 34a** the energy losses are calculated using the fitted profiles. In **Fig. 34b** the WDIA-signal is used. Only the data set investigating trends in effective mass with constant β_N is included.

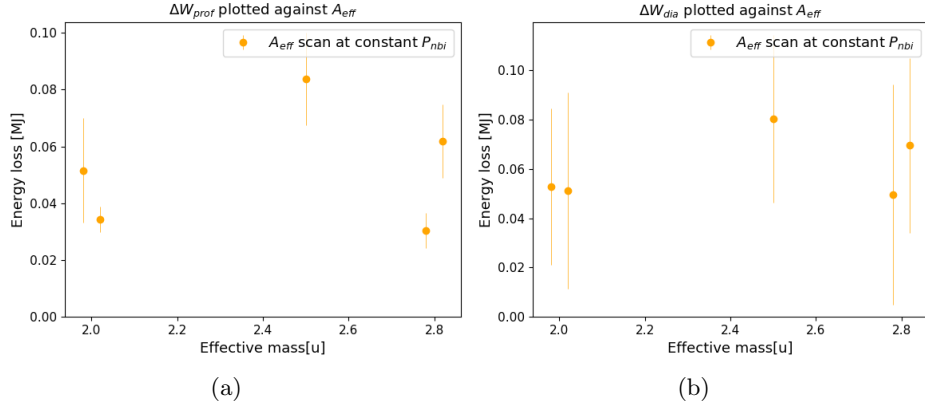


Figure 35: Energy losses plotted against effective mass. In **Fig. 35a** the energy losses are calculated using the fitted profiles. In **Fig. 35b** the WDIA-signal is used. Only the data set investigating trends in effective mass with constant power supply from neutral beam injection are included.

5 Discussion

Comparison between moving averages and average windows for diamagnetic signal

By comparing the two methods used to calculate ΔW_{dia} it is found, in **Sec. 4.1**, that the values from moving averages are 40 % larger on average. The reason is at least partially that it was typically used for a smaller set of data centered on the minimal level. Comparatively, the average windows method typically has wider windows in order to decrease the uncertainty. However, this also means that the time span also includes times where the energy is higher after the ELM. The difference can be seen by comparing **Fig. 13** and **Fig. 14** where there is a short period after the ELM where the energy is comparatively high. The moving average method does not include this span while the average windows method does. One way of making the methods more similar is to increase the time window used for moving averages. The problem then, is that the maximum post-ELM drop is very soon after the ELM. As a result, the time window might be stretched to include data from before the ELM. Additionally, the steep drop in energy means that the uncertainties would be inflated. Another way of getting more similar results is to shorten the time windows used for the average windows method. The problem is then that the ELMs do not always lose energy equally fast and some of the signal might be lost.

Which method is best might depend on what they are being compared to. As discussed in **Sec.4.2**, the average windows agree better with the results from the profiles method. Another way of evaluating the results is by comparison with previous experiments at similar collisionality as is done in **Fig. 22**. The average windows method already produces a result that is slightly large compared to previous experiments, the moving averages would be even larger. While it could be possible that the ELMs indeed are larger, the profiles method indicates that they are not.

Comparison between diamagnetic measurements and profiles method

The ratio between ΔW_{dia} and ΔW_{prof} for specific data points can serve as a measurement on how well the two methods agree with each other. As discussed in **Sec. 4.2** the ratio is close to 1, at least well within the uncertainty. This seems to imply that there is no significant systematic difference between the two methods. Another explanation could be that the systematic difference is cancelled out by a difference in the energy of ions and electrons in the plasma.

The uncertainty of the ratio can serve as a measurement on how precise the methods are. The large uncertainty seems to indicate that there is still room for improvement. Interestingly, by excluding the data points where ICRH has been used the uncertainty is almost halved. This might suggest that these data points are not as reliable. While it might be interesting to exclude these data points from future studies, there is not enough data to do so.

An interesting difference in the methods is that the post-ELM energy average is measured closer to the ELM in the diamagnetic signal. The reason for this is that the time windows for both methods were chosen to capture as much of the drop as possible. The ELM energy loss seems to be captured sooner in the diamagnetic signal as compared with the other diagnostics.

Scan in B_T , density, A_{eff} and gas rate

For the investigated parameters B_T , density, A_{eff} and gas fueling rate no clear trends were found. It seems unlikely that none of the parameters affect the characteristics of ELMs. One reason no trends are found could be that the deployed methods are unable to distinguish fine enough differences between ELMs. This seems likely as the uncertainties in a lot of the measurements are comparatively large. Another problem could be that the data is too noisy. This too seems likely. While the diamagnetic signal is consistently noisy, the quality of the TS, ECE and reflectometry data varies from pulse to pulse. Excluding noisy data is difficult as the data set is already limited.

Collisionality trend

The most important aspect of this work is finding whether the size of peeling ELMs are comparable to ballooning ELMs with similar collisionality. The data set did not have a large enough spread in collisionality to see any trend. The trend in collisionality is only apparent when collisionality varies between $10^{-1} - 10^1$ which is larger than what is included in the data treated in this work. However, as can be seen in **Fig. 22** and **23**, the results seem to align fairly well with observations in previous experiments. As such, the results from this work do not suggest that there is any significant difference in ELM size between peeling and ballooning ELMs. This is a very important result as it implies that extrapolations of trends to the operational mode of ITER are more likely to be valid.

Future studies

In order to find conclusive trends, more data is needed in order to make up for noise. Preferably, the data should cover a wider range of parameters where it is possible. It would be especially interesting to recreate peeling limited ELMs with a wider range of collisionality. Due to JET currently being closed down indefinitely these experiments would have to be held elsewhere. Using a different fusion device is difficult as it has different capabilities and the experiment has to be designed in another way.

However, more could possibly be done with data from this experiment. One important take away from this work is that the reflectometry diagnostic KG10 and ECE diagnostic KK3 perform very well. Their high time resolution means that they are able to create profiles for singular ELMs, which is impossible with the comparatively low time resolution of the TS diagnostic. While TS

measurements are still important for calibration, they do not have to be as close to the ELM as the data used for creating profiles has to be. Creating profiles for singular ELMs has multiple advantages. Perhaps most important is that the one does not have to assume that ELMs have the same characteristics in a time interval. While often true, this assumption is violated to varying degrees as exemplified in the case discussed in **Sec. 6.1**. While it might still be reasonable to bunch ELMs together to diminish the effect of uncertainties in measurements, fitting profiles to singular ELMs still has potential benefits. For one, it reduces problems of ELMs, indirectly, being weighed differently due to them having different influences on fitted curves. Secondly, if certain individual ELMs have different characteristics or obviously poor data quality, they could be treated separately. Lastly, normalization could be done for all individual ELMs which would give a more accurate normalization as it removes the influence of differences in pre-ELM profiles.

6 Appendix

6.1 Discussion on problematic time interval

The interval between 48.83 and 49.67s in shot 104417 has comparatively large ELM losses as calculated using temperature and density profiles. This section aims to discuss the validity of using the it as a data point.

Firstly, it should be mentioned that the interval only includes two ELMs, which is lower than any other investigated interval. This is reflected by the relatively small amount of data of interest in this interval which is shown in **Fig. 36**. Additionally, the data has a large spread. Especially the ECE data clearly has two distinct tracks that correspond to the two different ELMs. Similarly, the reflectometry data has a very large spread with the outer most data belonging to one ELM and the inner most to another ELM. Part of the reason why the ELM losses are larger from the profile method as compared to the diamagnetic signal is that the fit has overvalued the ELM with a higher pre-ELM profile. This can be seen in the density profile where the rebinned data (purple) mostly follows the highest density data points. In the post-ELM data the two ELMs are not as easily distinguishable. Which ELM gets overemphasized is partly random as it depends on how many scans are of a diagnostic are done during a time window. For most intervals this is not an issue as the ELMs are more similar and there is more data. This does not cause the same overestimation in ΔW_{dia} since it creates a fit to as it measures each ELM individually and weighs all ELMs equally.

In the end, the data point was kept in the all figures as there did not seem to be anything clearly wrong during the interval. Rather, the reason why this data point is an outlier is an unfortunate combination of a weakness in the method and randomness in the behaviour of the plasma. Additionally, the large errors associated with the data point indicate that it is not to be given too much credibility.

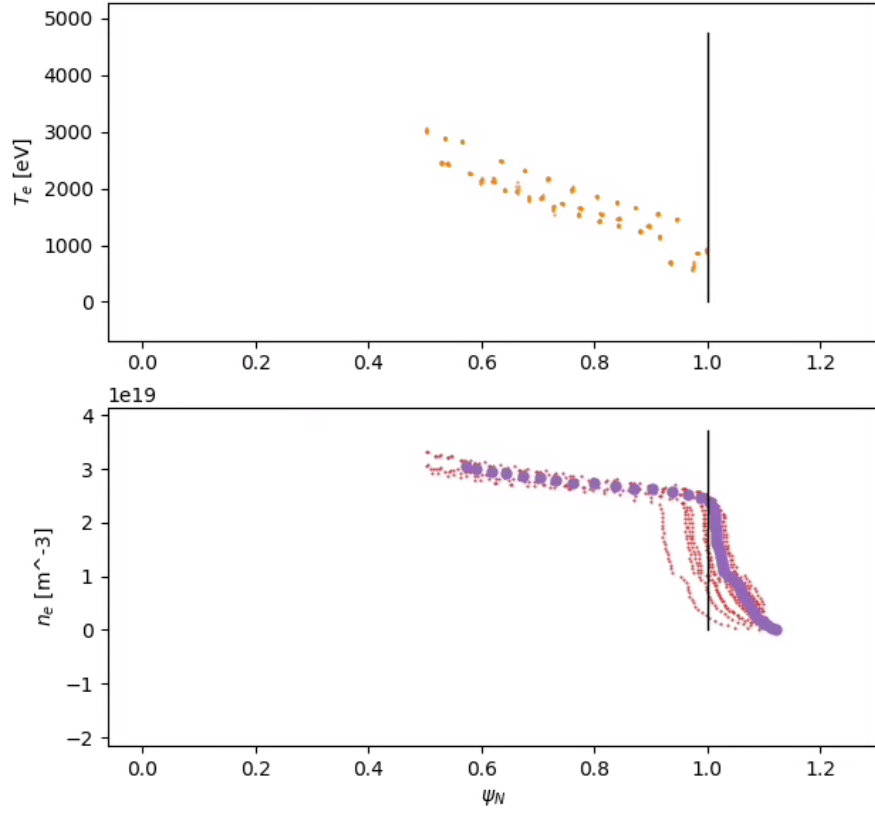


Figure 36: Temperature and density data used for fitting pre-ELM profiles for the interval 48.73-49.67s, shot 104417.

References

- [1] BP. Statistical review of world energy. 2019.
- [2] World Meteorological Organization. *The Global Climate 2011-2020: A decade of accelerating climate change*. WMO-No. 1338, 2021.
- [3] Directorate-General for Communication. UN Climate Change Conference: World agrees to transition away from fossil fuels and reduce global emissions by 43% by 2030, December 2023.
- [4] D. Fasel and M.Q. Tran. Availability of lithium in the context of future d-t fusion reactors. *Fusion Engineering and Design*, 75-79:1163–1168, 2005. Proceedings of the 23rd Symposium of Fusion Technology.
- [5] ITER. ITER - safety. <https://www.iter.org/mach/safety>, 2024. Accessed: 2024-05-14.
- [6] Arthur Stanley Eddington. *The Internal Constitution of the Stars*. Cambridge University Press, Cambridge, 1926.
- [7] Merlijn Jakobs. *Fusion Energy - Burning Questions*. PhD thesis, 11 2016.
- [8] EUROfusion. JET - Joint European Torus, 2024. Accessed: 2024-06-08.
- [9] ITER Organization. Iter - the machine, 2024. Accessed: 2024-05-21.
- [10] A Loarte et al. Characteristics of type i elm energy and particle losses in existing devices and their extrapolation to iter. *Plasma Physics and Controlled Fusion*, 45(9):1549, aug 2003.
- [11] ITER Organization. Tokamak. <https://www.iter.org/mach/Tokamak#:~:text=The%20term%20%22tokamak%22%20comes%20to,evacuated%20from%20the%20vacuum%20chamber.,> 2024. Accessed: 2024-05-21.
- [12] Wikipedia contributors. Toroidal and poloidal coordinates. https://en.wikipedia.org/wiki/Toroidal_and_poloidal_coordinates, 2024. Accessed: 2024-05-21. By DaveBurke - Own work, CC BY 2.5, <https://commons.wikimedia.org/w/index.php?curid=1169843>.
- [13] Gianmaria De Tommasi. Plasma magnetic control in tokamak devices. *Journal of Fusion Energy*, 38(3):406–436, 2019.
- [14] John Wesson and David J Campbell. *Tokamaks*, volume 149. Oxford university press, 2011.
- [15] Jeffrey P. Freidberg. *Plasma Physics and Fusion Energy*. Cambridge University Press, 2007. Accessed: 2024-05-21.
- [16] FusionWiki. <https://wiki.fusion.ciemat.es/wiki/Separatrix>. Accessed: April 24, 2024.

- [17] M Keilhacker. H-mode confinement in tokamaks. *Plasma Physics and Controlled Fusion*, 29(10A):1401, oct 1987.
- [18] F Wagner. A quarter-century of h-mode studies. *Plasma Physics and Controlled Fusion*, 49(12B):B1, nov 2007.
- [19] FusionWiki. <http://fusionwiki.ciemat.es/wiki/Pedestal>. Accessed: February 26, 2024.
- [20] Punit Gohil. Edge transport barriers in magnetic fusion plasmas. *Comptes Rendus Physique*, 7(6):606–621, 2006. Turbulent transport in fusion magnetised plasmas.
- [21] Maarten Vergote and Kristel Crombé. Radial electric fields and transport barriers. *Journal of Fusion Energy*, 42(3):123–145, 2023.
- [22] MNA Beurskens, A Alfier, B Alper, I Balboa, J Flanagan, W Fundamenski, E Giovannozzi, M Kempenaars, A Loarte, P Lomas, et al. Pedestal and scrape-off layer dynamics in elmy h-mode plasmas in jet. *Nuclear fusion*, 49(12):125006, 2009.
- [23] H Zohm. Edge localized modes (elms). *Plasma Physics and Controlled Fusion*, 38(2):105, feb 1996.
- [24] L. Frassinetti et al. Pedestal structure and stability at low collisionality in tcv. In *48th EPS Conference on Plasma Physics*. EPS, 2022.
- [25] Valentin Igochine. Physics and control of edge localized modes (elms), 2012. Lecture notes.
- [26] T. Pütterich et al. The iter baseline scenario investigated at asdex upgrade. In *27th IAEA Fusion Energy Conference (FEC 2018)*, 2018. Accessed: 2024-05-21.
- [27] O. Sauter, C. Angioni, and Y. R. Lin-Liu. Neoclassical conductivity and bootstrap current formulas for general axisymmetric equilibria and arbitrary collisionality regime. *Physics of Plasmas*, 6(7):2834–2839, 07 1999.
- [28] L. Frassinetti et al. Proceedings of the 50th eps conference on plasma physics. In *50th EPS Conference on Plasma Physics*, European Physical Society, July 2024. 4-12 July 2024.
- [29] L. Frassinetti et al. Peeling limited experiment in jet-ilw. In *Proceedings of the ITPA-PEP Meeting*, April 2024. Presentation at the ITPA-PEP meeting.
- [30] K. Miyamoto. *Plasma Physics and Controlled Nuclear Fusion*. Springer-Verlag, 2005.